Geosci. Model Dev. Discuss., 4, 3623–3690, 2011
www.geosci-model-dev-discuss.net/4/3623/2011/
doi:10.5194/gmdd-4-3623-2011


Geoscientific Model Development Discussions



# Evaluation of the sectional aerosol microphysics module SALSA implementation in ECHAM5-HAM aerosol-climate model

**T. Bergman[1,2], V.-M. Kerminen[2,3], H. Korhonen[1], K. J. Lehtinen[1,4], R. Makkonen[2], A. Arola[1], T. Mielonen[1], S. Romakkaniemi[4], M. Kulmala[2], and H. Kokkola[1]**

[1]Finnish Meteorological Institute, Kuopio Unit, Kuopio, Finland
[2]University of Helsinki, Department of Physics, Helsinki, Finland
[3]Finnish Meteorological Institute, Climate Change, Helsinki, Finland
[4]University of Eastern Finland, Department of Applied Physics, Kuopio, Finland

Received: 18 November 2011 – Accepted: 26 November 2011
– Published: 14 December 2011

Correspondence to: T. Bergman (tommi.bergman@iki.fi)

Published by Copernicus Publications on behalf of the European Geosciences Union.







## Abstract

We present the implementation and evaluation of a sectional aerosol microphysics model SALSA within the aerosol-climate model ECHAM5-HAM. This aerosol microphysics module has been designed to be flexible and computationally efficient so that it can be implemented in regional or global scale models. The computational efficiency has been achieved by keeping the number of variables needed to describe the size and composition distribution to the minimum. The aerosol size distribution is described using 20 size sections with 10 size sections in size space which cover diameters ranging from 3 nm to 10 µm divided to three subranges each having distinct optimised process and compound selection.

The ability of the module to describe the global aerosol properties was evaluated by comparison against (1) measured continental and marine size distributions, (2) observed variability of continental modal number concentrations, (3) measured sulphate, organic carbon, black carbon and sea salt mass concentrations, (4) observations of AOD and other aerosol optical properties from satellites and AERONET network, (5) global aerosol budgets and concentrations from previous model studies, and (6) model results using M7 which is the default aerosol microphysics module in ECHAM5-HAM.

The evaluation shows that the global aerosol properties can be reproduced reasonably well using the coarse resolution of 10 size sections in size space. The simulated global aerosol budgets are within the range of previous studies. Surface concentrations of sea salt, sulphate and carbonaceous species have an annual mean within a factor of five of the observations, while the simulated sea salt concentrations reproduce the observations less accurately and show high variability. Regionally, AOD is in relatively good agreement with the observations (within a factor of two). At mid-latitudes the observed AOD is captured well, while at high-latitudes as well as in some polluted and dust regions the modeled AOD is significantly lower than the observed.





GMDD

4, 3623–3690, 2011



Regarding the most investigated aerosol properties, the performances of SALSA and the modal aerosol module M7 against observations are comparable. However, SALSA reproduces the observed number concentrations and the size distributions of CCN sized particles much more accurately than M7, and is therefore a good choice for aerosol-cloud interaction studies in global models. Our study also shows that when including activation type nucleation process in the boundary layer, the modeled concentrations of particles under 50 nm in diameter are reproduced much better compared to when only binary nucleation is assumed.

## 1 Introduction

Aerosols and their interactions with clouds constitute the largest uncertainty in the estimation of present-day radiative forcing of the Earth's atmosphere (Forster et al., 2007; Myhre, 2009; Quaas et al., 2009), hindering seriously our ability to predict the future climate change (Schwartz et al., 2010). Reducing these uncertainties requires detailed information on the spatial and temporal variability of the concentration, number size distribution and chemical composition of aerosol particles throughout the atmosphere. Necessary tools for getting such detailed information are large-scale modeling frameworks together with various measurements platforms (Ghan and Schwartz, 2007).

Simulating the size-resolved chemical composition of atmospheric aerosols can be done in several ways. The most accurate and flexible in terms of the shape of the size distribution, yet computationally most demanding, method for this purpose is the sectional method (e.g. Jacobson, 2001; Adams and Seinfeld, 2002; Spracklen et al., 2005). In this approach the aerosol population is typically divided into a relatively large number of fixed size bins, and the particle number concentration and mass concentrations of different chemical constituents are being tracked separately for each size bin. The second commonly-used method is the modal method that describes the aerosol population with a few log-normal modes (e.g. Vignati et al., 2004; Stier et al., 2005; Pringle et al., 2010; Mann et al., 2010; Zhang et al., 2010). The modal approach is





GMDD
4, 3623–3690, 2011



typically much faster than the sectional method, but it has some challenges in describing accurately many climatically important processes, including cloud droplet activation and atmospheric new-particle formation and growth (Zhang et al., 1999). A more rarely-used approach is the moment method, in which all aerosol processes are tied into different moments of the particle number size distribution (e.g. Bauer et al., 2008). However, in the moment method, aerosol properties require a separate retrieval so this approach can be considered rather inconvenient for interpreting model simulations and comparing the simulations with atmospheric measurements.

Due to computational limitations, most existing large-scale modeling frameworks employ either a modal approach or, alternatively, some combination of modal and sectional or even bulk (only aeosol mass) approaches (e.g. Liu et al., 2005a; Reddy et al., 2005; Liao et al., 2009). The sectional model SALSA (Kokkola et al., 2008) was designed to reduce the computational burden of aerosol processes via the optimization of the model performance without losing physical features relevant to climate simulations. As a result, the width of size bins and the degree of internal mixing are not fixed but vary over the particle size range in SALSA. The number of chemical compounds and active processes modeled vary also from size bin to another. These simplifications reduce the computational burden significantly without neglecting any of the most significant processes or chemical compounds. Comparisons to a detailed aerosol model demonstrated that SALSA is capable of simulating accurately basic aerosol microphysical processes in a zero dimensional framework (Kokkola et al., 2008). The main advantage of SALSA compared to modal methods is that no pre-defined assumptions of the particle size distribution shape are used, which can significantly affect e.g. cloud activation predictions.

In this work, we present an evaluation of the SALSA model in the global general circulation modeling framework ECHAM5. We compare the aerosol representation of SALSA to that of the M7 modal model that is also implemented in ECHAM5 (Stier et al., 2005) and has been applied in several studies (e.g. Lohmann et al., 2007; Hoose et al., 2008; Sesartic et al., 2011; O'Donnell et al., 2011; Partanen et al., 2011). Our





GMDD
4, 3623–3690, 2011



comparison focuses on global aerosol budgets, aerosol optical properties and particle number size distributions. To assess the qualitative correctness of the representation, comparisons to in situ measurements and satellite observations are performed as well.

## 2 Model description

### 2.1 Aerosol-climate model ECHAM5-HAM

The atmospheric general circulation model ECHAM5 developed at Max Planck Institute for Meteorology is a fifth generation global climate model (Roeckner et al., 2003, 2004). The prognostic equations are solved as spherical harmonics with triangular truncation. In ECHAM5 the horizontal grid is discretised using the spectral transform method. Gridpoint calculations are done in a Gaussian grid. For vertical discretisation ECHAM5 uses the hybrid $\sigma$-pressure coordinates. In ECHAM5 the pressure ranges from 1013 hPa to 10 hPa. In this study we have used spectral truncation of 63 (corresponding to approximately $1.9^{\circ} \times 1.9^{\circ}$ on the gaussian grid) and 31 levels in the vertical. The time step for this resolution is 12 min. Large scale transport uses the Flux Form Semi-Langrangian (FFSL) method by Lin and Rood (1996).

The Hamburg Aerosol Model (HAM) (Stier et al., 2005) consists of emission, removal and microphysical parts. Emissions and removal processes are partly calculated online and partly prescribed. Aerosol microphysics are calculated using the M7 modal aerosol model by Vignati et al. (2004). In our study we have replaced the M7 model with SALSA model and compared the differences.

### 2.2 Nudging

Simulations are done using the nudging method described by Jeuken et al. (1996). The method relaxes the synoptic scale meteorology towards observed atmospheric conditions by using atmospheric re-analysis data, in our case the ECMWF (The European





GMDD
4, 3623–3690, 2011



Centre for Medium-Range Weather Forecasts) operational re-analysis data (Uppala et al., 2005). This technique is known to produce too slow wind speeds (Timmreck and Schulz, 2004) and thus produce too small amounts of wind-driven aerosols. Nevertheless, it is the best way to quantify the differences in aerosol population that are induced by the differences in the aerosol models within ECHAM5-HAM aerosol-climate model.

### 2.3 SALSA model

SALSA model describes the aerosol population with a moving center sectional approach (Jacobson, 1997b). SALSA is constructed to allow flexible modification of the amount of bins and their boundaries. In this study SALSA consists of 20 size sections, of which 10 are defined in size space with parallel size sections depending on the external mixing of different sized particles (see Fig. 1). These size sections cover diameters ranging from 3 nm to 10 µm. The diameter range is divided into three different subranges with three or four size sections. The size section boundaries within subranges are spaced logarithmically and the diameter limits between size sections are shown in Table 1. External mixing of particles is limited to subranges 2 and 3.

To reduce the computational burden the handling of processess affecting different sections has been simplified. Simplifications include confining compounds and processes in order to include only the most relevant ones in the given size range. Processes are listed in Table 2. The subranges and their compounds have been described in Table 3. In the third subrange only number concentrations and mass concentration of water soluble material are considered. The prognostic variables include a particle number concentration for each section and a mass concentration for particles in sections below 700 nm. As mass is not a prognostic variable in subrange 3 the sectional mean diameter is fixed.

Aerosol number and mass mixing ratios are transported as tracers for subranges 1 and 2, while only number mixing ratio tracer is transported for 3rd subrange. In the 3rd subrange the aerosol radii are constrained to the mean volume of a given size section. Compounds included in the model are sulphate (SU), organic carbon (OC), black





GMDD
4, 3623–3690, 2011



carbon (BC), sea salt (SS) and dust (DU). In addition to these compounds there is a water soluble mass tracer in subrange 3c which includes all water soluble compounds.

Subrange 1 consists of three sections and there are no parallel size sections. This section consists mainly of freshly nucleated particles with a particle diameter between 3 nm and 50 nm. The particle compounds include only sulfate and organic carbon.

Particles in subrange 1 are grown by condensation and lost by wet deposition and by coagulation with larger particles.

Particles with diameter between 50 nm and 700 nm reside in subrange 2. This subrange has two externally mixed bins for each of the four size sections. The externally mixed sections are separated by their solubility which represents their ability to act as cloud condensation nuclei. Wet deposition is a significant removal process for these particles. This subrange involves all compounds: organic and black carbon, sulphate, sea salt and mineral dust. Soluble bins include all compounds while the insoluble sections include all compounds except sea salt.

The three size sections in subrange 3 have a particle range from 700 nm to 10 µm. All the three size sections have three parallel bins. Most of the particles originate from natural sources. There are three externally mixed subranges: sea salt, soluble dust, and insoluble dust. The remaining water soluble compounds are treated as one compound (water soluble – WS) within the insoluble dust group. The particle dry diameter is fixed in this subrange. Number concentration and the mass of water soluble material are the only prognostic variables.

### 2.4 Microphysical processes

One of the computationally most expensive processes in modeling the aerosol population is coagulation. Therefore, coagulation is calculated for each bin so that particles will only collide with larger particles. However, there is an exception for subrange 2b where particles can also collide with particles in the same parallel size bin in subrange 2a. Collisions where both colliding particles have diameters exceeding 700 nm the calculation is omitted due to small coagulation coefficients (Seinfeld and Pandis, 2006).





GMDD
4, 3623–3690, 2011



The mass transfer of gaseous $H_2SO_4$ onto particle surfaces is calculated using Analytical Predictor of Condensation scheme (Jacobson, 1997a) with the saturation vapor pressure set to zero. For collision rate expression we use the one in Lehtinen et al. (2004). For simultaneous calculation of nucleation and condensation we use the operator splitting technique developed by Jacobson (2002).

The equilibrium wet diameter of particles in different size bins are calculated using the ZSR method (Stokes and Robinson, 1966). To reduce the computational burden hydration is calculated only for soluble size bins. We use binary molalities for inorganic salts in the calculation of hydration using parameterisations given by Jacobson (2005). For organics we assume ideal behaviour.

### 2.4.1 New particle formation

Particle number in the atmosphere can increase in two different ways: as primary particles by emission or as secondary particles by going through the gas-particle transformation-nucleation. For the calculation of nucleation the current setup has three optional mechanisms in the boundary layer: parameterised sulphuric acid-water binary homogeneous nucleation parameterisation (Vehkamäki et al., 2002), and two empirical parameterisations for kinetic (Sihto et al., 2006; Riipinen et al., 2007) and activation nucleation (Kulmala et al., 2006; Riipinen et al., 2007). The binary nucleation is applied to whole atmosphere with an exception in the cases with empirical parameterisations. In these cases the empirical parameterisations substitute the binary nucleation in the boundary layer.

Both activation-type and kinetic-type nucleation parameterisations calculate the 1 nm particle formation rate as a function of sulphuric acid concentration

$$J_1 = K[H_2SO_4]^l, \quad (1)$$

where $K$ is the empirically defined activation (or kinetic) coefficient (for activation-type nucleation we have used $K = 1 \times 10^{-7}\ s^{-1}$; Sihto et al., 2006; Riipinen et al., 2007) and /





GMDD
4, 3623–3690, 2011



is the nucleation exponent, which is 1 for activation (or 2 for kinetic) nucleation scheme. The binary homogeneous nucleation is parameterised as a function of temperature, relative humidity and sulphuric acid as described by Vehkamäki et al. (2002).

Nucleation produces particles that have a diameter of approximately 1 nm. As the smallest section in SALSA has a lower limit of 3 nm, the growth of these freshly nucleated particles from 1 nm to 3 nm by molecular collisions and condensation must be calculated before the particles can be inserted in the section 1a1. To calculate the growth we have implemented three different parameterisations developed by Kerminen and Kulmala (2002), Lehtinen et al. (2007) and Anttila et al. (2010). Kerminen and Kulmala (2002) calculate the growth of 1 nm particles by condensation. Lehtinen et al. (2007) improve the applicability of the Kerminen and Kulmala (2002) parameterisation for wider range of atmospheric conditions. The Anttila et al. (2010) parameterisation includes the condensational growth together with self-coagulation. The effect of these parameterisations is not compared and will be a subject for a future study. In this study we have used the Kerminen and Kulmala (2002) parameterisation. This parameterisation has the form

$$J_3 = J_1 \exp\left(\gamma \frac{\mathrm{CS}}{\mathrm{GR}}\right), \tag{2}$$

where $J_1$ and $J_3$ are the nucleation rates of 1 nm and 3 nm particles. $\gamma$ is a parameter calculated on-line depending on particle population and temperature. CS is the condensation sink, the surface of other aerosol particles consuming condensing vapors and GR is the nuclei growth rate calculated from the concentrations of condensable vapors according to Kerminen and Kulmala (2002).

Other new particle formation schemes (e.g. participation of organic vapors) will also be a subject of a future study.





GMDD
4, 3623–3690, 2011



### 2.4.2 Chemistry

The sulphur cycle is based on the sulphur cycle model by Feichter et al. (1996). The considered gas phase sulphur compounds are dimethylsulfide (DMS), sulphur dioxide ($SO_2$) and sulphuric acid ($H_2SO_4$).

The prescribed 3-D oxidant fields of OH, $H_2O_2$, $NO_2$, $O_3$ are calculated with the comprehensive MOZART model by Horowitz et al. (2003). Gas phase DMS and $SO_2$ are oxidised by hydroxyl (OH), and additionally DMS reacts with nitrate radicals ($NO_3$). Aqueous phase oxidation of $SO_2$ by $H_2O_2$ and $O_3$ is considered. The aqueous phase concentration of $SO_2$ is calculated using Henry's law accounting for dissolution effects.

Sulphate produced in gas-phase is allowed to condense on existing particles or to nucleate. Sulphate produced in-cloud is distributed into available pre-existing particles in subranges 2a and 3a. Existing number mixing ratios are used to calculate the fraction of sulphate to insert in a subrange. Within a subrange the mass is distributed evenly into all sections. In case of no pre-existing particles all of the sulphate mass is converted into number mixing ratio and placed in subrange 3a.

### 2.4.3 Repartitioning of number and mass concentrations

In M7, particles are transfered to soluble mode when there is one mono-layer coating of soluble material on them (see Vignati et al., 2004). In SALSA, the move requires a predefined fraction of soluble material to condense on the particles before they are transfered to the soluble bin which is of the same diameter. The critical soluble fraction for each bin is calculated using Köhler theory using supersaturation of 0.5 % (Kokkola et al., 2008). While this is implemented in the model, in this study the repartitioning is not used.

In SALSA, the compounds have mass tracers only in subranges 1 and 2, and therefore the growth of particles over the boundary between 2nd and 3rd subrange has to be treated separarely. When particles grow over the boundary, all mass mixing ratios





GMDD
4, 3623–3690, 2011



in 2a4 are transferred to 3b1. The corresponding particle number mixing ratio is calculated from the transferred mass using the fixed bin mean diameter. Also growth over the boundary of subrange 2b is calculated in similar fashion. The insoluble material from 2b4 is transfered to 3c1 and converted to number concentrations using bin mean diameter. However, for the soluble material in subrange 2b there is water soluble mass tracer associated with the subrange 3c. The soluble mass fraction from 2b4 is transferred to water soluble fraction of 3c1 during growth over the subrange boundary.

A more detailed description of SALSA can be found in Kokkola et al. (2008)

### 2.5 Removal processes

#### 2.5.1 Wet deposition

Wet deposition is the removal of trace gases and aerosols by clouds and precipitation. Implementation of this process includes re-evaporation and subsequent release of aerosols back to the atmosphere as well as in-cloud and below cloud scavenging. Removal of $SO_2$, DMS and $H_2SO_4$ by precipitation and clouds is calculated using Henry's law (see e.g. Seinfeld and Pandis, 2006).

Aerosols are scavenged by clouds through activation of aerosols as cloud condensation nuclei (CCN). However, the activation of aerosols to CCN is not calculated explicitly in the used model version. Instead their removal is parameterized using solubility of different compounds using method described in Stier et al. (2005). The change of tracer $i$ is calculated with

$$\frac{\Delta C_i}{\Delta t} = \frac{R_i C_i f^{\mathrm{cl}}}{C_{\mathrm{wat}}} \left( \frac{Q^{\mathrm{liq}}}{f^{\mathrm{liq}}} + \frac{Q^{\mathrm{ice}}}{f^{\mathrm{ice}}} \right) \tag{3}$$

where $R_i$ is the size and composition dependent scavenging parameter for aerosols. $C_i$ and $C_{\mathrm{wat}}$ are the mixing ratios of particles and total cloud water, respectively. $f^{\mathrm{cl}}$ is the cloud fraction, $f^{\mathrm{liq}}$ and $f^{\mathrm{ice}}$ are the liquid and ice fraction of cloud water. $Q^{\mathrm{liq}}$ and $Q^{\mathrm{ice}}$ are the respective sums of conversion rates of cloud liquid water and cloud ice water





GMDD
4, 3623–3690, 2011



to precipitation through auto-conversion, aggregation and accretion. The calculation is unchanged from Stier et al. (2005) where a more detailed description can be found. Coefficients $R_i$ for SALSA follow Stier et al. (2005) and are shown in Table 4. As the coefficients are essentially the same for SALSA and M7, the variations in removal rates for aerosols depend mainly on the simulated cloud patterns.

Aerosols below a precipitating cloud are removed from the atmosphere by rain droplets. Their removal depends on aerosol concentration, collection efficiency and area of precipitation. Largest effect on below cloud scavenging is caused by size dependent collection efficiency of rain and snow which follows the one presented in Seinfeld and Pandis (2006, see Ch. 20).

### 2.5.2 Dry deposition

Dry deposition velocity is calculated using serial resistance analogy. The resistance analogy calculates the deposition velocity as inverse of resistance of the surface $v_d = r^{-1}$, where the resistance $r$ is parameterised by the surface properties. The scheme of Ganzeveld and Lelieveld (1995) and Ganzeveld et al. (1998) is used. Dry deposition flux is calculated using

$$F_d = C \rho_{air} v_d, \quad (4)$$

where $C$ is the number mixing ratio, $\rho_{air}$ is the air density and $v_d$ is the dry deposition velocity. Key obstacle in calculating the dry deposition flux is to calculate the deposition velocity, which ties together all relevant processes involved. The total apparent resistance of the surface is divided into three parts: aerodynamical $r_a$, quasi-laminar $r_b$ and surface $r_s$ resistances. The aerodynamic resistance $r_a$ is calculated in ECHAM5. The quasi-laminar, or boundary layer, resistance is determined from the kinematic viscosity of the air. And the third term, surface resistance, is prescribed for most of the trace gases. Only for $SO_2$, it is calculated by parameterisation of pH, relative humidity, surface temperature and the canopy resistance (Stier et al., 2005). Total resistance is the sum of the three resistances.





GMDD
4, 3623–3690, 2011



Aerosol particle dry deposition for both M7 and SALSA uses the big leaf method with $r = r_a + r_s$. The aerosol deposition is calculated on-line using the bin number and mass to calculate the aerosol deposition velocity as a function of particle radius, density, turbulence and surface cover as in Stier et al. (2005). More detailed calculation is presented in Kerkweg et al. (2006).

### 2.5.3 Sedimentation

Aerosol particles within the atmosphere are drawn towards the surface by gravitation – this process is known as sedimentation. Sedimentation velocity is calculated using Stokes law (Seinfeld and Pandis, 2006)

$$F = \frac{3\pi\mu R_p U_\infty}{C_c}, \quad (5)$$

where $R_p$ is the particle radius, $\mu$ is air viscosity, $u_\infty$ is wind velocity and $C_c$ is the Cunningham slip correction factor. For particle radius and diameter we use bin mean radius in similar way as M7 uses the mode mean radius.

The calculation of sedimentation relies on the radii of the particles, and as the particles in different sections can be internally mixed, the deposition velocities for different internally mixed compounds are the same. As the sedimentation velocity might break the Courant-Friedrich-Lewy stability criterion the sedimentation velocity is limited to $v \leq \frac{\Delta z}{\Delta t}$, where $\Delta t$ is the timestep length and $\Delta z$ is the model layer thickness.

## 2.6 Emissions

The emission module has been rewritten to produce input suitable for a sectional model, while keeping the emission routines otherwise intact. Sea salt, dust and oceanic DMS emissions are calculated on-line. For anthropogenic emissions we have used AeroCom year 2000 emission inventory (Dentener et al., 2006) with modifications by Stier et al. (2005), even though the simulation runs were made using meteorology for year





GMDD
4, 3623–3690, 2011



2008. As both M7 and SALSA runs have emissions for the same year this should not cause significant differences between the experiments. However, when comparing to actual observations for year 2008 the emissions from year 2000 may cause discrepancies.

### 2.6.1 Carbon emissions

Carbonaceous emissions in particle phase have been mapped to sectional space so that all carbonaceous mass is emitted in subranges 1a, 2a or 2b. The mapping is calculated using lognormal distributions by Stier et al. (2005) with median particle radius $\bar{r} = 0.075$ and standard deviation $\sigma = 1.59$ which are adapted from the distributions by Dentener et al. (2006) which have $\bar{r} = 0.04$ and $\sigma = 1.8$.

There are three different emission sources for black carbon: biofuel, wildfire, and fossil fuel. Black carbon is assumed to be insoluble, and as such it is emitted to sections within subrange 2b only.

For organic carbon there are four different sources: biogenic, vegetation fire, biofuel and fossil fuel. 65 % of the biomass burning is assumed to be water soluble (Mayol-Bracero et al., 2002) and emitted to subranges 1a or 2a. This organic carbon is mostly emitted through vegetation fires. The remaining 35 % is emitted as insoluble particles to subrange 2b.

### 2.6.2 Sulphur emissions

Sulphur is emitted to the atmosphere mainly as $SO_2$ from natural and anthropogenic sources. Naturally sulphur is emitted to the atmosphere mainly by continuous and explosive volcanic activity. Also a large natural source of $SO_2$ is its precursor dimethylsulfide emitted from both oceanic and terrestial sources. Anthropogenic sources of $SO_2$ include wild fires, fossil fuel and biomass burning.

Emissions from volcanic sources are based on GEIA inventory (http://www.igac.noaa.gov/newsletter/22/sulfur.php; http://www.geiacenter.org/) (Andres and Kasgnoc,





GMDD
4, 3623–3690, 2011



1998). Sulphur emission size dependence from anthropogenic sources follow the modal structure published by Dentener et al. (2006). However, in HAM emissions are adapted to use the M7 modal parameters (Stier et al., 2005). For the interest of this comparison the emissions are mapped to SALSA sectional structure using the M7 modal parameters.

Most of the anthropogenic sulphur – 97.5 % – is emitted as $SO_2$ and 2.5 % is emitted as particulate $SO_4$ (Dentener et al., 2006). The primary emissions of $SO_4$ are emitted to subranges 1a, 2a and 3b. Sulphur is emitted to second lowest model level. Original $1^\circ \times 1^\circ$ gridded data is remapped to model resolution $1.9^\circ \times 1.9^\circ$ using area weighted averaging.

Emissions of oceanic DMS are calculated on-line by using Nightingale et al. (2000) parameterization for air-sea exchange transfer velocities using simulated 10 m wind speeds. Continental DMS emissions are prescribed as reported by Pham et al. (1995).

### 2.6.3 Sea salt emissions

The sea salt emission scheme has been rewritten and therefore we provide a more detailed description of its emission than for other compounds.

Sea spray droplets are produced by mechanical tearing of waves or by bursting of bubbles on the sea surface (e.g. de Leeuw et al., 2011). These mechanisms can be expressed with several different sea spray generation functions that can be found in the literature. Usually these formulas provide parameterisation of the emission flux as a function of 10 m wind speed. Guelle et al. (2001) show that the formulation of Monahan et al. (1986) is best suited for small particle range ($r_{dry}$ below 4 µm). However, Gong (2003) has found out that for particles under 0.2 µm radius using the Monahan et al. (1986) parameterisation overestimates the number flux and has formulated a new parameterisation for these small particles. For particles with dry radius above 4 µm and below 20 µm the formulation of Smith and Harrison (1998) or Andreas (1998) should be used. We have used the Andreas (1998) formulation for these larger particles. We calculate the emission flux into 2nd and 3rd sub ranges, and hence we use all





GMDD
4, 3623–3690, 2011



three parameterisations. In the following formulae $r$ stands for radius at RH 80 %. For the smallest sea salt emission in the radii range from 50 nm to 400 nm emissions are calculated using the Gong (2003) parameterisation

$$\frac{dF}{dr} = 1.373 U_{10}^{3.41} r^{-A} (1 + 0.057 r^{3.45}) 10^{1.607 e^{-B^2}}, \quad \text{when } 0.05\,\mu\text{m} \le r \le 0.4\,\mu\text{m}, \tag{6}$$

where $A = 4.7(1+\Theta r)^{-0.017 r^{-1.44}}$ and $B = (0.433 - \log\ r)/0.433$. $\Theta$ is a fitting parameter that can be used to adjust the emissions below 0.2 µm. $U_{10}$ is the windspeed at 10 m height. According to Gong (2003) changing the parameter $\Theta$ from 30 to 15 can increase the number concentrations as much as one order of magnitude and values 30–40 produce similar emissions. Hence, we have used $\Theta = 30$ which will cause underestimation rather than overestimation.

In the 400 nm to 8 µm range the flux is calculated using Monahan et al. (1986)

$$\frac{dF}{dr} = 1.373 U_{10}^{3.41} r^{-3} (1 + 0.057 r^{1.05}) 10^{1.19 e^{-B^2}}, \quad \text{when } 0.4\,\mu\text{m} \le r \le 8\,\mu\text{m}, \tag{7}$$

where $B = (0.380 - \log\ r)/0.650$

For the largest particles with radii over 8 µm we use the Andreas (1998) parameterisation

$$\frac{dF}{dr} = C U_{10} r^{-1}, \quad \text{when } r \ge 8\,\mu\text{m}, \tag{8}$$

where parameter $C$ is calculated by assigning Eq. (7) at its upper limit equal with Eq. (8) at its lower limit.

Following these parameterisations we calculate the number and mass fluxes using 10 m wind speeds in the range from 0 to 32 m s$^{-1}$. The fluxes are calculated by integrating over each section separately The number flux within a section is calculated from the mass flux using sectional mean diameter.





GMDD
4, 3623–3690, 2011



### 2.6.4 Dust emissions

Mineral dust is found throughout the atmosphere either as fine grained silt or as coarse grained minerals. Mineral dust is lifted to the atmosphere by the surface winds. Higher wind speeds increase the amount and also the size of emitted dust particles.

Dust emissions are calculated using the parameterisation by Tegen et al. (2002). Dust flux is calculated online using 10 m wind speeds, soil clay content and soil moisture from ECHAM5. Both SALSA and M7 use the same parameterisation. The Tegen et al. (2002) parameterisation calculates the flux in sectional space which is mapped to M7 modal structure. To produce minimal differences between the models, we use the M7 modal formulation of the flux, which is then mapped to SALSA sections. Mineral dust is emitted to subranges 2b and 3c.

## 2.7 Radiation

Calculation of aerosol optical properties is computationally very expensive and is therefore unfeasible to be done online. Instead the needed aerosol properties have been calculated beforehand for 24 spectral bands as shown by Toon and Ackerman (1981). These precalculated values are provided as lookup tables for the ECHAM5-HAM with three dimensions: Mie parameter $\alpha = 2\pi r/\lambda$, real and imaginary refractive indices $n_r$ and $n_i$. For the Mie parameter we have $r$ as the mean radius of a section and $\lambda$ as the wavelength. The compound specific complex refractive indices $n_r$ and $n_i$ are shown in Table 5.

Each bin can have varying amounts of different compounds. Therefore we approximate $n_r$ and $n_i$ by volume weighted average of the refractive indices of individual compounds including aerosol water. As reported by Lesins et al. (2002) the error of AOD in the extreme case of black carbon and water can reach up to 15 %.

From the lookup tables the model retrieves the extinction cross section, single scattering albedo and assymmetry factor. Using these values the aerosol optical depth and Ångström exponent are then calculated for each bin at each grid point and each level.





GMDD
4, 3623–3690, 2011



## 3 Comparison to other model studies

### 3.1 Budgets of aerosol species

Aerosol budgets and lifetimes give us an overview of the cycling of different compounds. The compound specific global aerosol budget varies both spatially and temporally.

We have compared the simulated global budget of aerosols between SALSA and M7. To ease the comparison we have also provided corresponding values reported by Liu et al. (2001) and Textor et al. (2006). As Textor et al. (2006) focus on particulate species we have included the Liu et al. (2001) for reference of the gaseous species within the sulphur cycle. The overview of aerosol lifecycles is presented in Tables 6 and 7. Table 6 summarises the global sulphur cycle for ECHAM5-HAM with SALSA and M7 and Table 7 summarises the aerosol budget for black carbon, organic carbon, sea salt and dust.

#### 3.1.1 Sulphur

The sulphur cycle presented in Table 6 is relatively unchanged with the SALSA microphysics when compared to the cycle of M7. Overall, the burdens of sulphur compounds are nearly identical to those simulated with M7.

Simulated burden of particulate $SO_4$ is the same with SALSA and M7 at 0.64 Tg(S). It is only 0.02 Tg (3.0 %) smaller than the amount reported in AeroCom comparison where the mean for 16 models is 1.99 Tg($SO_4$) which corresponds to 0.66 Tg(S) (Textor et al., 2006, see Table 10.). SALSA shows four times higher mass of nucleated $SO_4$ than M7. This is partly explained by the model structure. In SALSA the nucleated mass of sulphur includes also the sulphur consumed by growth of freshly nucleated particles from approximately 1 nm to 3 nm in diameter.

For the particulate $SO_4$ the difference between the models is caused mainly by aqueous chemistry where the $SO_2$ is oxidised in clouds to produce particulate $SO_4$.





GMDD
4, 3623–3690, 2011



Additionally there are small differences in condensation, which contributes roughly one quarter of the particulate phase sulphur. The condensation is only 0.62 Tg (2.7 %) higher than with M7. While the pathways to particulate $SO_4$ are clearly different, the global average burdens for $SO_4$ particles are the same with both models. On the one hand dry deposition of $SO_4$ with SALSA and M7 is lower than reported by either Liu et al. (2005b) or AeroCom. On the other hand wet deposition with SALSA is at the upper bound of the model spread reported by Liu et al. (2005b). Despite the mismatch between SALSA and AeroCom or SALSA and Liu et al. (2005b) the total sink is almost the same as in AeroCom comparison and within the variation of Liu et al. (2005b). The lower sources therefore seem to be compensated with lower sinks.

The overall burden of sulphur associated with gas phase $H_2SO_4$ $7\times10^{-4}$ Tg is 22 % smaller than with M7. This difference is caused by differences in sources and sinks. While M7 uses all the available $H_2SO_4$ for condensation and nucleation, in SALSA the amount depends on the equilibrium mass transfer between particles and gas phase $H_2SO_4$.

The burden of $SO_2$ is 0.23 Tg (26.4 %) lower than with M7, but 0.03 Tg (5.0 %) higher than maximum burden reported by Liu et al. (2005b). The aqueous oxidation from $SO_2$ to particulate $SO_4$ is 11.41 Tg (19.0 %) lower with SALSA. Differences in aqueous oxidation, however, are probably caused by differences in the low-level cloud cover between the model runs (see the cloud cover in Table 6) and do not necessarily indicate differences induced by the different microphysics. Cloud cover of low level clouds (below 750 hPa) for SALSA run is 3.7 % lower than with M7 which causes lower aqueous oxidation of $SO_2$ (see the cloud cover in Table 6). The oxidation of $SO_2$ with OH is clearly (51.6 %) higher with SALSA than with any of the models included in the study by Liu et al. (2005b). This may be a result from inefficient wet and dry deposition of $SO_2$ (39.7 % and 13.5 % lower than with M7), which are at the low end of variation reported by Liu et al. (2005b). The produced $H_2SO_4$ might be overestimated as a result of high oxidation of $SO_2$ with OH. However, the more detailed study of the $SO_2$ dynamics are beyond the scope of this study.





GMDD
4, 3623–3690, 2011



DMS emissions are calculated online using the simulated 10 m windspeeds, and despite the nudging method, the global annual mean 10 m wind speeds are 4 % lower with SALSA. The lower windspeeds cause 11 % lower emissions of DMS with SALSA. As DMS is globally a large source of sulphur, lower DMS leads to slightly lower mass of $SO_2$ and $SO_4$. However, the emissions with SALSA are at the upper bound of the variation in the emission of DMS as reported by Liu et al. (2005b).

### 3.1.2 Organic carbon

As the prescribed emissions of organic carbon are the same for SALSA and M7, there is no difference between the models. Atmospheric burden of organic carbon (OC) at 0.96 Tg differs only 0.03 Tg (3 %) from the burden simulated with M7 (0.93 Tg). As the organic carbon mass is associated only with subranges 1 and 2, this suggests that most of the OC is in particles below 700 µm in diameter. In AeroCom comparison the mean of particulate organic matter is found to be 1.7 Tg which corresponds to 1.21 Tg (OC) being 21 % higher than with SALSA. While the burden is practically the same for both models, the lower removal of organic carbon indicates that part of the mass is transfered to subrange 3 and thus implies that the burden should be even little higher with SALSA. Underestimation of organic carbon mass is expected as organic carbon mass is underestimated in most global aerosol-climate models (Jathar et al., 2011) .

For organic carbon the sinks are 20 % (11.55 Tg) lower with SALSA, because with SALSA the mass of individual compounds is lost when particles grow larger than 700 nm. This is also seen as lower sedimentation of organic carbon particles, which mainly affects very large aerosols. This leads to sedimentation being 2.5 times smaller because only sedimentation of OC is tracked only for particles under 700 nm.

### 3.1.3 Black carbon

Similarly to organic carbon the emissions are the same with both models. The burden of black carbon is 0.07 Tg which is 0.03 Tg lower than that of M7. Both models have





GMDD
4, 3623–3690, 2011



simulated burden lower than in any of the studies mentioned by Liu et al. (2005b) and clearly lower than the mean of the models participating in AeroCom intercomparison. However, even in the AeroCom comparison ECHAM5-HAM has the lowest BC burden of all models which is probably due to lower emissions of carbonaceous material than in the other models. Similarly to organic carbon the removal of black carbon is lower in SALSA than in M7 being less than half of the emitted mass. Removal being clearly lower than emission implies that relatively large portion of particles are grown to subrange 3 and the actual burden might be within the variation reported by Liu et al. (2005b). The growth of black carbon to 3rd subrange is partly caused by low removal of insoluble particles by wet deposition thereby increasing the time for growth of particles.

### 3.1.4 Sea salt and mineral dust

As a large portion of the mass of sea salt and mineral dust is in particles larger than 700 nm in diameter, the mass of these particles is estimated using the mean diameter of particles and their densities.

Sources for sea salt are significantly higher with SALSA which is caused by the new formulation of sea salt emissions while differences in wind patterns may also play a role. The burden of sea salt is quite similar for both models. However, the sedimentation is 66 % higher with SALSA. As dry and wet depositions are of similar magnitude (within 9 % and 22 % respectively) in both models. The emissions are clearly higher with SALSA mainly due to higher wind speeds at the Southern Ocean. Despite the 1200 Tg difference for the emission of sea salt particles, the burden is only 0.83 Tg (6.6 %) smaller with SALSA. It seems that the large difference in emissions is compensated by larger sedimentation with SALSA.

With dust, however, emission and burden are clearly lower with SALSA than with M7. The emissions with SALSA are less than half (44 %) of the emissions with M7. SALSA emissions are similarly less than half of the amount reported in the AeroCom emission inventory (Dentener et al., 2006). The difference is caused by 7 % lower surface wind speeds over land with SALSA and the calculation of emissions using modal parameters





GMDD
4, 3623–3690, 2011



for SALSA bin structure. Dry removal processes are still quite comparable (9 % lower), and the main difference in the total removal rate is due to wet deposition. In SALSA mineral dust is mainly emitted to insoluble bins and therefore has weaker wet deposition flux. Also the removal by dry deposition and sedimentation is low especially when comparing with AeroCom comparison. This might be influenced by fixed bin diameters in the sub region 3 as sedimentation velocity is dependent on the particle diameter.

Water soluble fraction in the subrange 3c constitutes very small part of total aerosol loading. Global burden is only 0.0087 Tg which is in the same range as gas phase $H_2SO_4$.

### 3.2 Lifetimes

We calculated the lifetime of particles by using a relation between source and burden rather than sink and burden. We chose this way because part of the aerosol mass is transferred to subrange 3 which does not include mass tracers. However, there will be some error because the burden does not include particles larger than 700 nm in diameter for OC, BC and $SO_4$.

The lifetimes of black carbon and sea salt are lower with SALSA, but otherwise M7 predicts longer lifetimes. For black carbon and dust the difference in lifetimes between models exceeds one day.

Lifetimes for the simulated compounds except black carbon are within the variation reported in the AeroCom intercomparison (Textor et al., 2006). In all cases SALSA is within the variation shown in Liu et al. (2005b).

The largest difference to AeroCom multimodel mean is found in black carbon, which is most probably caused by the coagulation or growth losses to particles larger than 700 nm in diameter. Lower burden and lower removal by dry and wet deposition and sedimentation could indicate that a large fraction of the material is removed by the processes only after growing over 700 nm boundary in the aerosol model.





GMDD
4, 3623–3690, 2011



Even though the sea salt emissions are higher, the lifetime of particles is shorter than with M7, because the removal rate of sea salt is increased. The increase in removal is mainly due to higher sedimentation in SALSA than in M7, thereby resulting in 21.6 % smaller lifetime than with M7.

For dust the lifetime with SALSA is 2.45 days lower than with M7 but the proportional significance of different removal processes are rather consistent with M7 while the emissions are less than half of those simulated with M7 and little less than in other studies previously reported (Liu et al., 2005b; Textor et al., 2006).

### 3.3 Spatial distribution of aerosol mass

Figure 2 shows the annual mean of vertically integrated column mass of the compounds in particulate phase. Aerosol mass distribution of different compounds varies depending on the properties of the compound as can be seen in Fig. 2. Removal and transport depends largely on the composition of particles, and particles consisting of mainly water soluble material are more prone to be removed by wet deposition, and fine insoluble particles will more probably be transported further from the source.

Sulphate is seen in large areas over both land and ocean. The wide dispersal of $SO_4$ results from $SO_2$ dispersion throughout the atmosphere and its oxidation to $H_2SO_4$ and consequent nucleation and condensation. Regions with highest burdens for organic carbon coincide with strong emission areas as most of the global organic carbon is found in the South America and Central Africa. The column burden of sea salt is naturally high over the oceans. However, there are also relatively high burdens in some parts of e.g. Australia, South-America and East-Coast of Africa indicating transport towards inland.

Sea salt burden is highest in the Southern Ocean, area which has reportedly very high windspeeds (Yuan, 2004) producing large amounts of sea salt. By comparing sea salt and aerosol water burdens in Fig. 2d and 2f we can see that a large part of aerosol water is associated with sea salt aerosols.





GMDD
4, 3623–3690, 2011



Dust burden is highest near large deserts. Most prominently the dust emissions from deserts are seen over Sahara while also Asian and Australian deserts show large dust burden. The transport of Saharan dust all the way to Amazonia can be seen and the transport of Saharan mineral dust to Amazonia has also been observed by Gilardoni et al. (2011).

### 3.4 Vertical distribution

In Fig. 3 we show the annual mean of the zonally averaged number concentrations for SALSA (left hand panels) and M7 (right hand panels). The M7 number concentrations are calculated for SALSA subrange diameter ranges to facilitate comparison. Additionally we have plotted the M7 number concentrations of particles below the lower limit of SALSA in the topmost panel on the right hand side.

In the panel (a) we can see that especially in the upper troposphere the binary nucleation creates extremely high amount of particles that do not show up in SALSA due to their inability to grow over 3 nm in diameter, which is the low cut off diameter of SALSA's size distribution.

With M7 the concentrations of particles 3–50 nm in diameter are between 2000–10 000 at the maximum while SALSA has concentrations as much as ten times higher with 10 000–50 000 $cm^{-3}$ in the upper troposphere. Additionally the high concentrations extend to somewhat lower pressures. The difference for particles 3–50 nm in diameter between SALSA and M7 is caused primarily by different treatment of the smallest particles. In SALSA the sub-3 nm particle growth has been parameterised while M7 has a nucleation mode that extends to this size range. As much of the condensating vapor $H_2SO_4$ is used for nucleation in M7, the particles do not grow enough to show up in the 3–50 nm range.

In the 200 hPa region of subrange 2, SALSA has concentrations of 20–100 $cm^{-3}$ while M7 has concentrations below 10 $cm^{-3}$. This difference is probably a result from having four bins in SALSA and one or two modes with M7, thereby producing more accurate description for removal processes. In addition, with SALSA the particle





GMDD
4, 3623–3690, 2011



concentrations in the boundary layer are higher at high latitudes with concentrations of 20 to 50 $cm^{-3}$ as compared to 0 to 10 $cm^{-3}$ of M7. Near the equator the concentration maximums are closer, but still SALSA shows more particles than M7.

In the 3rd subrange the concentrations are relatively similar with both models. However, with SALSA the particles are transported higher and M7 shows slightly higher concentrations in the 200–600 hPa region.

In the southern hemisphere (60° S to 30° S) the surface concentrations with M7 are higher in this size range. There SALSA shows only 2–5 $cm^{-3}$ while M7 has values 2–10 $cm^{-3}$ thus SALSA has roughly halved concentrations. In this region most of the particles are sea salt and it seems that in SALSA the sea salt particles are larger and fewer, which may be caused by the fixed diameters used in the 3rd diameter range.

## 4 Comparison to surface measurements

### 4.1 Surface concentrations of particulate mass

We have compared the simulated and the observed annual mean surface mass concentrations (Fig. 4) of sulphate, organic carbon, black carbon and sea salt at measurement stations within European Monitoring and Evaluation programme (EMEP; http://www.emep.int) and United States Interagency Monitoring of Protected Visual Environment (IMPROVE; http://vista.cira.colostate.edu/improve/) networks. The scatterplots show the simulated concentrations in the lowest model layer in the gridboxes corresponding to measurement site locations. From IMPROVE network we have included data for 169 sites which correspond to 117 different gridpoints. To avoid comparing one gridpoint to more than one observation we have averaged the station data in cases where more than one station corresponds to a single gridpoint. From the EMEP network we found only 11 sites with data for year 2008 and from these only 7 had data for organic carbon and all 11 had data for black carbon. The sulphate and sea salt concentration data for EMEP stations were not available for year 2008. The observed





GMDD
4, 3623–3690, 2011



data includes the mass concentrations of particles smaller than 2.5 µm in diameter. The modeled mass concentration of sulphate, organic and black carbon is accounted for particles under 700 nm in diameter while the modeled mass concentrations of sea salt includes all smaller than 1.7 µm in diameter (bins 2a1–3a1).

In the organic carbon mass concentrations (Fig. 4a) we can see that SALSA underestimates the surface concentrations. Out of the 117 comparison pairs in 45 (36.5 %) the simulated concentrations are within a factor of two within the IMPROVE network data. In only 12 (10.3 %) cases the discrepancy is over one order of magnitude. Simulated concentrations fall within one order of magnitude in all of the seven EMEP sites. For both IMPROVE and EMEP the mean of simulated mass concentrations (0.80 $\mu g\,m^{-3}$ and 1.02 $\mu g\,m^{-3}$, respectively) are within a factor of two and three, respectively, of the observed mean (1.05 $\mu g\,m^{-3}$ and 2.79 $\mu g\,m^{-3}$). M7 shows slightly lower mean concentrations (0.73 $\mu g\,m^{-3}$ for IMPROVE and 0.93 $\mu g\,m^{-3}$ for EMEP) than SALSA. However, there are only seven datapoints in EMEP comparison reducing the representability of the average.

The black carbon mass concentration mean (Fig. 4b) for gridpoints corresponding to IMPROVE sites is 0.15 $\mu g\,m^{-3}$ (0.16 $\mu g\,m^{-3}$ with M7) which is 23 % lower than the observed mean of 0.20 $\mu g\,m^{-3}$. In 43 of the 117 cases (36.7 %), the simulated concentration is within a factor of two of the observed concentration. There are 17 gridpoints where the concentration differs more than 10-times from the observed. Thus at IMPROVE sites there is large variation, while on average the model captures concentrations quite well. The simulated mean of black carbon mass for EMEP sites is 0.39 $\mu g\,m^{-3}$ (0.38 $\mu g\,m^{-3}$ for M7) underestimating the observed mean of 0.85 $\mu g\,m^{-3}$ by 54 %. The over- and underestimation is strong at some of the EMEP and IMPROVE sites. The black carbon budget suggests that the underestimation is partly due mass associated with particles with diameter over 700 nm (Table 7).

In Fig. 4c scatterplot of $SO_4$ is shown. In 58 (49.6 %) cases the concentration is within a factor of two of the observations. The concentration of $SO_4$ has a mean of 0.75 $\mu g\,m^{-3}$ (0.66 $\mu g\,m^{-3}$ with M7). It is within a factor of two of the mean of observed





GMDD
4, 3623–3690, 2011



concentrations (1.27 $\mu g\,m^{-3}$). The concentrations exceeding 1 $\mu g\,m^{-3}$ are underestimated using SALSA with largest underestimation reaching over one order of magnitude at three gridpoints. However, the modeled sulphate mass is only accounted to 700 nm while the observations include particles up to 2.5 µm which partly explains the low concentrations.

Sea salt mass concentrations (Fig. 4d) exhibit high variation. The simulated concentrations have a mean of 0.045 $\mu g\,m^{-3}$ (0.16 $\mu g\,m^{-3}$ with M7) underestimating the observed mean of 0.13 $\mu g\,m^{-3}$ by 65 %. Of the 117 cases only 36 (30.8 %) are within a factor of two of the observed concentrations. The overall variation in sea salt concentrations is high and the discrepancy between observed and simulated concentrations can be as much as two orders of magnitude. The underestimation in larger particles may be partly due to the coarse bin structure and partly by limitd transport.

### 4.2 Particle size distributions and concentrations in Europe

Asmi et al. (2011) have collected aerosol measurement data for European Integrated Project on Aerosol Cloud Climate Air Quality interactions (EUCAARI; Kulmala et al., 2009, 2011) project sites for year 2008. We have compared a subset of these measurements to simulated size distributions simulated with SALSA and M7. Figure 5 shows the modeled and observed annual median aerosol size distributions together for six EUCAARI sites: Jungfraujoch (Jurányi et al., 2011), Hyytiälä (Hari and Kulmala, 2005), Mace Head (Jennings et al., 1991), Aspvreten (Tunved et al., 2004), Melpitz (Engler et al., 2007) and Pallas (Lihavainen et al., 2008). These sites include coastal (Mace Head), mountain (Jungfraujoch), arctic (Pallas), boreal coniferous (Hyytiälä), urban polluted (Melpitz) and mixed boreal coniferous and deciduous (Aspvreten) locations. For SALSA we have plotted the size distributions using binary and activation nucleation mechanisms while for M7 only binary nucleation mechanism is available.

By using the activation-type boundary layer nucleation the concentration of small particles is increased. Size distribution modeled with SALSA using activation-type





GMDD
4, 3623–3690, 2011



nucleation in the boundary layer shows better agreement with observations of particles smaller than 50 nm in diameter than with binary nucleation, which is in-line with earlier studies with activation-type nucleation(e.g. Spracklen et al., 2010; Kazil et al., 2010). Contrary to activation-type nucleation, the concentrations produced using binary nucleation by either of the models show significantly lower concentrations than observed. At the selected sites there is little or no difference in concentrations of particles larger than 80 nm in diameter between binary or activation-type nucleation with SALSA. Thus the concentrations of these particles depend heavily on the emissions and the higher concentrations of small particles with activation-type nucleation do not grow to larger sizes. The growth of nucleation mode particles could be increased with the inclusion of organic vapors.

Both SALSA and M7 show similar concentrations when using binary nucleation at four of the six sites. While at Jungraujoch and Mace Head the Aitken mode particles have very low concentrations with SALSA. The concentration of these particles is increased when using activation-type nucleation. However, the increased concentrations of these particles have very limited effect on the concentration of paticles 50 nm–100 nm in diameter.

In Fig. 5 panels c, d and e we see that the concentrations of particles 200 nm in diameter are clearly higher with SALSA than with M7. At these sites SALSA is closer to observed concentrations while it has trouble predicting the concentrations of particles 50 nm–100 nm in diameter seen in observations and simulation with M7. This is possibly caused by scavenging of small particles by coagulation and too low condensational growth of smaller particles.

The particles 100 nm–500 nm in diameter contribute most of the cloud condensation nuclei, therefore this size range is important for cloud activation studies. The cloud activation occurs mainly in diameter range 50 nm–200 nm and compared to M7, SALSA shows better agreement to observations for these particles in polluted regions and similar agreement in regions with clean air. However, the concentrations remain lower than observed, which is mainly caused by the missing condensation of organic vapors





GMDD
4, 3623–3690, 2011



which has been shown to have large impact on the growth of particles in this size range by Riipinen et al. (2011).

Figure 6 shows the histograms of concentrations of 100–500 nm particles ($N_{100}$) at six EUCAARI stations. The particle diameter of 100 nm corresponds roughly to activation at critical supersaturation of 0.3 % for Finnish background aerosol (Sihto et al., 2010). In four cases SALSA shows wider frequency of concentrations with higher frequencies at the larger concentrations than M7. In Mace Head the higher concentrations associated with polluted air are not reproduced with either models while the concentrations associated with marine air are well reproduced with SALSA. This supports the good agreement between SALSA and observations in the marine distributions (Fig. 8). In Pallas and Hyytiälä M7 shows histograms slightly closer to observed than SALSA, although the histograms with both models are similar. Overall, SALSA seems to produce histograms of the particles at size range relevant to cloud actication closer to observed than M7 indicating its better applicability to cloud activation studies. However, at sites with cleaner air (Pallas and Hyytiälä) M7 performs better further indicating that with too low growth of particles above 50 nm in diameter, $N_{100}$ depends largely on emissions.

The inclusion of organic vapors should increase the number of particles in diameter range important for cloud activation. The importance of influence of organic vapors on the cloud condensation nucleii concentrations is emphasised in clean environments. While both models underestimate size range relevant for cloud activation, SALSA performs slightly better and it is more suitable for cloud activation studies than M7. Nevertheless, the effect of organic vapors should be studied before the implementation of cloud activation of particles.

### 4.3 Marine particle number size distributions

Heintzenberg et al. (2000) have compiled marine boundary layer (MBL) aerosol size distributions of three decades of cruise and flight measurements. In their work the size distribution data has been presented as a log-normal bimodal distribution with geometric mean diameter, standard deviation and concentration on both modes. The





GMDD
4, 3623–3690, 2011



distributions have been reported for 10 different latitude bands. We have plotted the observed data together with simulated concentrations for SALSA and M7 (Figs. 7 and 8).

Figure 7 shows the average surface concentrations of particles larger than 20 nm in diameter for 10 different latitude bands. SALSA and M7 concentrations are averaged from the same regions as the observations (Fig. 1 in Heintzenberg et al. (2000)). The observed mean values are in the range 370–500 $cm^{-3}$ while the simulated values can reach over 1500 $cm^{-3}$ in the Southern Ocean. There we can see the largest discrepancy as the simulated particle concentrations for SALSA are 4-fold over the observed values. In the tropics SALSA and M7 show similar concentrations of particles. Still the concentrations with SALSA are higher than those with M7 in almost all latitude bands. The largest difference is seen in the Southern Ocean where SALSA produces five times higher concentrations of particles larger than 20 nm in diameter than M7. This difference is seen because measurement locations between Antarctica and South America coincide with a regions with high concentrations of sulphuric acid. The high amount of sulphuric acid causes stronger growth of freshly formed particles by condensation with SALSA than with M7, resulting in high concentrations of particles 20 nm–50nm in diameter. While on average M7 is underestimating the concentrations with 320 $cm^{-3}$ the new sea salt formulation of SALSA is overestimating the number concentrations with mean of 670 $cm^{-3}$ over the observed mean of 450 $cm^{-3}$. Despite overpredicting the mean concentration, SALSA mostly shows better agreement than M7. Furthermore, SALSA captures the concentrations at the roaring fourties (40°–49° S) much better than M7.

Simulated and observed particle size distributions in Fig. 8 are shown for annual mean surface concentrations in 12 latitude bands using gridpoints corresponding to the 15° × 15° gridboxes as explained by Heintzenberg et al. (2000). SALSA shows much better agreement with observed concentrations than M7. Especially for the particles with diameters 0.1 µm–1µm SALSA shows better agreement with the observations than M7. Moreover, SALSA reproduces the magnitude of the observed concentrations quite





GMDD
4, 3623–3690, 2011



accurately. Both models show high concentrations of small particles in the Southern Ocean. While the larger diameter mode seen in the observations has much lower concentrations with M7 it is produced more accurately with SALSA. Additionally SALSA has high concentrations of small particles. This is also seen as the overestimation of particle concentration in the Southern Ocean (Fig. 7). However, these small particles do not include sea salt and thus are produced by nucleation rather than by emission from the ocean.

## 5 Comparison to remote sensing observations

### 5.1 Aerosol optical depth

The simulated aerosol optical depth (AOD) is compared with satellite and ground-based measurements. The satellite retrievals include both the Moderate Resolution Imaging Spectrometer (MODIS) (Remer et al., 2005) and Multi-angle Imaging Spectro-Radiometer (MISR) (Martonchik et al., 1998) instruments. Because the MODIS AOD over land areas has high uncertainties (Levy et al., 2010; Pinty et al., 2010) we use a composite of the MODIS and the MISR instruments. The MODIS is used for ocean and MISR for land gridpoints. Ground-based measurements are gathered from the AERONET robotic network of sunphotometers (Holben et al., 1998).

MODIS and MISR level 3 data which have a spatial resolution of $1 \times 1$ degree were downloaded from NASA's Giovanni (Acker and Leptoukh, 2007) web portal (http://daac.gsfc.nasa.gov/giovanni/). The composite MODIS-MISR annual mean is calculated from monthly mean values.

The globally averaged aerosol optical depth for SALSA run with binary nucleation is 0.08 which is clearly lower than 0.12 calculated with M7. When calculating the AOD for gridpoints with available MODIS-MISR data the global annual average for satellite composite is 0.16. Mean AOD for gridpoints with satellite composite data is 0.11 with SALSA and 0.15 with M7. While the AOD at high latitudes is approximately the same





GMDD
4, 3623–3690, 2011



with both models, the AOD at the tropics is lower with SALSA resulting with lower global mean AOD.

Figure 9a shows the observed clear sky annual mean aerosol optical depth (AOD) composite of the satellite retrievals. Figure 9b shows the difference with SALSA to satellite retrieval, while Fig. 9c has the difference with M7. Although the SALSA global annual mean aerosol optical depth is smaller than satellite retrieval the spatial distribution is quite good. The AODs over ocean gridpoints in the tropics are generally within 0.02 of the satellite retrieval (Fig. 9). With both models the high latitudes have much lower AOD than satellite retrievals, especially over Siberia in Russia and in the coast of Alaska the AOD is underpredicted. The AOD is lower probably partly due to old emission inventory and partly due to too low transport (Bourgeois and Bey, 2011) from tropics and mid-latitudes towards the poles. Furthermore, MODIS sees a band of higher AOD around Antarctica which the models do not reproduce. However, the differences in this area are partly caused by the cloud fraction affecting the satellite aerosol retrieval (Shi et al., 2011).

Overall, the differences to observations at higher latitudes are similar between the models while in the tropics and partly in the mid-latitudes, especially over oceans, M7 has AOD at least 0.05 higher than SALSA. Furthermore, in the Saharan dust bloom over North Atlantic Ocean M7 shows AOD 0.15 higher than observed while SALSA shows only 0.02 difference to observed AOD (Fig. 9). Over Siberia and Canada both models are underpredicting clearly with 0.2 smaller values than in MISR retrieval. In Europe and the east coast of USA the AOD with SALSA is captured mainly within 0.02 of the observed while M7 shows differences over 0.05.

In a sensitivity test we found that replacing the M7 modal standard deviations with those suggested by Dentener et al. (2006) (see Sect. 2.6.1) the AOD between Africa and South America rose at most by 0.02 (not shown). However, this has only 0.001 effect on the global annual mean AOD. Similarly, activation-type nucleation has no effect on the AOD despite the increase in 50 nm particles. This is expected because their effect on the concentration of particles larger than 200 nm is very low (see Fig. 5).





GMDD
4, 3623–3690, 2011



Even though M7 achieves to produce better agreement in terms of overall average, this is because M7 underpredictions at high-latitudes are compensated with overpredictions at mid-latitudes. The underprediction at high-latitudes is seen with both models and is probably due to low transport of aerosols towards the poles as stated earlier. The low transport of aerosols to polar regions is a well documented problem with several global aerosol models (Shindell et al., 2008; Koch et al., 2009; Korhonen et al., 2008).

In Fig. 10 we show the AERONET (Holben et al., 2001) robotic network level 2 data for AOD for 42 sites with monthly mean data for 2008. The simulated data are plotted as box plots against five observed AOD ranges. SALSA shows somewhat lower variation compared to M7 with a lower median in all ranges. The AOD at aeronet sites is mainly below 0.3 and for these occurrences both models show mostly AODs within the range. In the smallest range from 0.0 to 0.1 SALSA is underestimating slightly less than M7. For the AOD from 0.1 to 0.2 SALSA is underestimating and having lower extreme values compared to M7. In all the three smallest AOD classes where the observed AOD is under 0.3 the median for SALSA is 0.10 which is lower than AERONET AOD of 0.12. M7, however, has a median AOD of 0.14 which is higher than either SALSA or AERONET. Both models underestimate the observed values exceeding 0.3. Usually the high AOD corresponds to extreme events such as dust blooms and are often underpredicted with global models. However, the most frequent small AODs are reproduced relatively accurately.

### 5.2 Ångström exponent

Figure 11 shows the Ångström exponent over oceans for SALSA, M7 and MODIS. The uncertainty of MODIS instrument is large over land and therefore we have inclued the Ångström exponent only over oceans (Mielonen et al., 2011). The Ångström exponent

$$\mathrm{ANG} = \frac{\ln \mathrm{AOD}_1 - \ln \mathrm{AOD}_2}{\ln \lambda_2 - \ln \lambda_1} \quad (9)$$





GMDD
4, 3623–3690, 2011



provides information on the absorption and scattering of radiation depending on the aerosol size within the air column. Smaller numbers indicate higher optical importance of coarse particles while larger Ångström exponent indicates stronger influence of accumulation particles on the radiative transfer. Mean for MODIS over oceans is 0.74 while the models show much higher Ångström exponent with 1.39 and 1.13 for M7 and SALSA, respectively. As the Ångström exponent is a qualitative parameter the overall distribution of the parameter is more important than its exact values. SALSA has similar spatial distribution with the satellite retrieval over oceans as the smallest Ångström exponent values are found over the Southern Ocean and west of Sahara. However, the magnitude is clearly too low indicating that over oceans there should be fewer large particles than either of the models predict.

## 6 Conclusions

In this study we have implemented and evaluated the Sectional Aerosol module for Large Scale Applications (SALSA) within aerosol-climate model ECHAM5-HAM. SALSA consists of an optimised sectional structure with 20 sections having 10 sections in size space. Simulated constituents include sulphate, organic carbon, black carbon, sea salt and dust. The differences to the HAM default aerosol microphysical model M7 have been descibed in detail. The major difference to M7 (or any modal model) is that in SALSA no assumptions of the size distribution shape are made, which is a great advantage especially in modeling cloud droplet activation and/or new particle formation. For the evaluation we have simulated the aerosol population for year 2008. The number and mass concentrations are compared with other models and observations.

The global annual mean aerosol column burdens fall mostly within results from other models included in AeroCom intercomparison (Textor et al., 2006) and Liu et al. (2005b). On average the surface mass concentrations of organic carbon, black carbon $SO_4$ and sea salt are close to observed but slightly underestimated. In case of organic carbon, black carbon and $SO_4$ changes of emissions of these material between 2000





GMDD
4, 3623–3690, 2011



and 2008 play a clear role. This should be investigated by using emission inventories and observations for the same year including observations from South America, Asia and Africa.

Annual median size distributions with binary nucleation show similar concentrations as M7. However, for both models the concentrations are almost one order of magnitude lower than observed (Fig. 5). For the simulation run with activation-type boundary layer nucleation the concentration of particles smaller than 50 nm in diameter shows better agreement with observations than with binary nucleation. However, the growth of these particles is too low and 50 nm to 200 nm diameter particle concentrations are lower than observed. One reason for too limited growth is the lack of organic vapors in this study. The effect of organic vapors on the growth of particles will be studied in the future. The frequencies of 100 nm to 500 nm (important size range for cloud activation) particle concentrations (Fig. 6) show somewhat infrequent high concentrations with SALSA although compared to M7 the histograms are closer to observed. Therefore SALSA is a good choice for studying cloud activation in aerosol-climate models. Latitudinal annual mean aerosol concentrations over Oceans capture the observed size distributions well (Fig. 8). The agreement with observations is especially good for particles 0.1–1.0 µm in diameter.

Although the concentrations of particles smaller than 50 nm in diameter are increased with activation-type nucleation the change in AOD remains negligible, which is supported with the concentrations of optically active particles remaining very close to those produced by binary nucleation.

The modeled global annual mean AOD with SALSA was found to be lower than the composite of satellite retriavals and lower than AERONET. The most significant contributions to global AOD come from Saharan dust and from polluted areas in India and China. However, the simulated AOD is in good agreement with MODIS-MISR satellite composite over tropical Oceans and parts of EU and USA with SALSA (Fig. 9). With the high-latitude AOD being underestimated and tropical AOD close to satellite retrievals the global annual mean AOD is underpredicted. Therefore the aerosol





GMDD
4, 3623–3690, 2011



emissions and transport into polar regions needs to be studied in the future. Nevertheless, very few number of sections is needed to produce AOD close to observed especially over oceans. This is achieved by carefully selecting correct bin widths, compositions and external mixing in the size distribution.

Ångström exponent distribution has lowest values over the Southern Ocean and west of Saharan desert as also seen with MODIS retrieval, indicating large sea salt particle contribution in these areas while also Saharan desert dust affects the Ångström exponent.

Although in many aspects SALSA performs adequately further improvement is needed: (1) the growth of particles 50–300 nm in diameter is underestimated and the effect of organic vapors on the growth should be investigated in the near future. (2) The poleward transport of aerosols depends largely on their removal by wet deposition. Thus the calculation of wet deposition should be modified for the sparse sectional structure. (3) The mass of different compounds should be investigated using emissions and observations for the same year and broaden the observations to include all the continents. In addition, the change of using sectional distribution of emissions instead of M7 modal parameters should be investigated. (4) Recent advances in remote sensing of vertical distribution of aerosols as well as in-situ measurements onboard aircrafts should be used to validate the vertical distribution of aerosols in SALSA.

*Acknowledgements.* This work was supported by the Academy of Finland (project 119741). We thank Ari Asmi for providing the observational size distribution data for EUCAARI measurement sites and Max Planck Institute for Meteorology for access to ECHAM5-HAM model.

## References

Acker, J. G. and Leptoukh, G.: Online Analysis Enhances Use of NASA Earth Science Data, Eos, Trans. AGU, 88, 14 and 17, 2007. 3653

Adams, P. J. and Seinfeld, J. H.: Predicting global aerosol size distributions in general circulation models, J. Geophys. Res., 107, 4370, doi:10.1029/2001JD001010, 2002. 3625





GMDD

4, 3623–3690, 2011



Andreas, E. L.: A New Sea Spray Generation Function for Wind Speeds up to 32 m $s^{-1}$, J. Phys. Oceanogr., 28, 2175–2184, doi:10.1175/1520-0485(1998)028<2175:ANSSGF>2.0.CO;2, 1998. 3637, 3638

Andres, R. J. and Kasgnoc, A. D.: A time-averaged inventory of subaerial volcanic sulfur emissions, J. Geophys. Res., 103, 25251–25261, doi:10.1029/98JD02091, 1998. 3636

Anttila, T., Kerminen, V.-M., and Lehtinen, K. E.: Parameterizing the formation rate of new particles: The effect of nuclei self-coagulation, J. Aerosol Sci., 41, 621–636, doi:10.1016/j.jaerosci.2010.04.008, 2010. 3631

Asmi, A., Wiedensohler, A., Laj, P., Fjaeraa, A.-M., Sellegri, K., Birmili, W., Weingartner, E., Baltensperger, U., Zdimal, V., Zikova, N., Putaud, J.-P., Marinoni, A., Tunved, P., Hansson, H.-C., Fiebig, M., Kivekäs, N., Lihavainen, H., Asmi, E., Ulevicius, V., Aalto, P. P., Swietlicki, E., Kristensson, A., Mihalopoulos, N., Kalivitis, N., Kalapov, I., Kiss, G., de Leeuw, G., Henzing, B., Harrison, R. M., Beddows, D., O'Dowd, C., Jennings, S. G., Flentje, H., Weinhold, K., Meinhardt, F., Ries, L., and Kulmala, M.: Number size distributions and seasonality of submicron particles in Europe 2008–2009, Atmos. Chem. Phys., 11, 5505–5538, doi:10.5194/acp-11-5505-2011, 2011. 3649, 3684

Bauer, S. E., Wright, D. L., Koch, D., Lewis, E. R., McGraw, R., Chang, L.-S., Schwartz, S. E., and Ruedy, R.: MATRIX (Multiconfiguration Aerosol TRacker of mIXing state): an aerosol microphysical module for global atmospheric models, Atmos. Chem. Phys., 8, 6003–6035, doi:10.5194/acp-8-6003-2008, 2008. 3626

Bourgeois, Q. and Bey, I.: Pollution transport efficiency toward the Arctic: Sensitivity to aerosol scavengin and source regions, J. Geophys. Res., 116, D08213, doi:10.1029/2010JD015096, 2011. 3654

de Leeuw, G., Andreas, E. L., Anguelova, M. D., Fairall, C. W., Lewis, E., O'Dowd, C., Schulz, M., and Schwartz, S. E.: Production flux of sea spray aerosol, Rev. Geophys., 49, RG2001, doi:10.1029/2010RG000349, 2011. 3637

Dentener, F., Kinne, S., Bond, T., Boucher, O., Cofala, J., Generoso, S., Ginoux, P., Gong, S., Hoelzemann, J. J., Ito, A., Marelli, L., Penner, J. E., Putaud, J.-P., Textor, C., Schulz, M., van der Werf, G. R., and Wilson, J.: Emissions of primary aerosol and precursor gases in the years 2000 and 1750 prescribed data-sets for AeroCom, Atmos. Chem. Phys., 6, 4321–4344, doi:10.5194/acp-6-4321-2006, 2006. 3635, 3636, 3637, 3643, 3654

Downing, H. D. and Williams, D.: Optical-constants of water in infrared, J. Geophys. Res., 80, 1656–1661, 1975. 3675





GMDD

4, 3623–3690, 2011



Engler, C., Rose, D., Wehner, B., Wiedensohler, A., Brüggemann, E., Gnauk, T., Spindler, G., Tuch, T., and Birmili, W.: Size distributions of non-volatile particle residuals ($D_p < 800$ nm) at a rural site in Germany and relation to air mass origin, Atmos. Chem. Phys., 7, 5785–5802, doi:10.5194/acp-7-5785-2007, 2007. 3649

Feichter, J., Kjellström, E., Rodhe, H., Dentener, F., Lelieveldi, J., and Roelofs, G.-J.: Simulation of the tropospheric sulfur cycle in a global climate model, Atmos. Environ., 30, 1693–1707, doi:10.1016/1352-2310(95)00394-0, 1996. 3632

Forster, P., Ramaswamy, V., Artaxo, P., Berntsen, T., Betts, R., Fahey, D. W., Haywood, J., Lean, J., Lowe, D. C., Myhre, G., Nganga, J., Prinn, R., Raga, G., Schulz, M., , and Van Dorland, R.: Climate Change 2007: The Physical Science Basis. Contribution of Working Group I to the Fourth Assessment Report of the Intergovernmental Panel on Climate Change, chap. Changes in Atmospheric Constituents and in Radiative Forcing, Cambridge University Press, Cambridge, United Kingdom and New York, NY, USA, 2007. 3625

Ganzeveld, L. and Lelieveld, J.: Dry deposition parameterization in a chemistry general circulation model and its influence on the distribution of reactive trace gases, J. Geophys. Res., 100, 20999–21012, doi:10.1029/95JD02266, 1995. 3634

Ganzeveld, L., Lelieveld, J., and Roelofs, G.-J.: A dry deposition parameterization for sulfur oxides in a chemistry and general circulation model, J. Geophys. Res., 103, 5679–5694, 1998. 3634

Ghan, S. J. and Schwartz, S. E.: Aerosol properties and processes. A path from field and laboratory measurements to global climate models, Bull. Am. Meteor. Soc., 88, 1059–10832, 2007. 3625

Gilardoni, S., Vignati, E., Marmer, E., Cavalli, F., Belis, C., Gianelle, V., Loureiro, A., and Artaxo, P.: Sources of carbonaceous aerosol in the Amazon basin, Atmos. Chem. Phys., 11, 2747–2764, doi:10.5194/acp-11-2747-2011, 2011. 3646

Gong, S. L.: A parameterization of sea-salt aerosol source function for sub- and super-micron particles, Global Biogeochem. Cy., 17, 1097, doi:10.1029/2003GB002079, 2003. 3637, 3638

Guelle, W., Schulz, M., Balkanski, Y., and Dentener, F.: Influence of the source formulation on modeling the atmospheric global distribution of sea salt aerosol, J. Geophys. Res., 106, 27509–27524, doi:10.1029/2001JD900249, 2001. 3637

Hari, P. and Kulmala, M.: Station for Measuring Ecosystem-Atmosphere Relations (SMEAR II), Boreal Env. Res., 10, 315–322, 2005. 3649

Heintzenberg, J., Covert, D. C., and van Dingenen, R.: Size distribution and chemical compo-





GMDD
4, 3623–3690, 2011



sition of marine aerosols: a compilation and review, Tellus, 52B, 1104–1122, 2000. 3651, 3652, 3687
Hess, M., Koepke, P., and Schult, I.: Optical properties of aerosols and clouds: The software package OPAC, Bull. Am. Meteorol. Soc., 79, 831–844, 1998. 3675
Holben, B., Eck, T. F., Slutsker, I., Tanre, D., Buis, J. P., Setzer, A., Vermote, E., Reagan, J. A., Kaufman, Y. J., Nakajima, T., Lavenu, F., Jankowiak, I., and Smirnov, A.: AERONET-A federated instrument network and data archive for aerosol characterization, Remote Sens. Environ., 66, 1–16, 1998. 3653
Holben, B. N., Tanré, D., Smirnov, A., Eck, T. F., Slutsker, I., Abuhassan, N., Newcomb, W. W., Schafer, J. S., Chatenet, B., Lavenu, F., Kaufman, Y. J., Castle, J. V., Setzer, A., Markham, B., Frouin, D. C. R., Halthore, R., Karneli, A., O'Neill, N. T., Pietras, C., Pinker, R. T., Voss, K., and Zibordi, G.: An emerging ground-based aerosol climatology: Aerosol optical depth from AERONET, J. Geophys. Res., 106, 12067–12098, 2001. 3655
Hoose, C., Lohmann, U., Stier, P., Verheggen, B., and Weingartner, E.: Aerosol processing in mixed-phase clouds in ECHAM5-HAM: Model description and comparison to observations, J. Geophys. Res., 113, D07210, doi:10.1029/2007JD009251, 2008. 3626
Horowitz, L. W., Walters, S., Mauzerall, D. L., Emmons, L. K., Rasch, P. J., Granier, C., Tie, X., Lamarque, J.-F., Schulz, M. G., Tyndall, G. S., Orlando, J. J., and Brasseur, G. P.: A global simulation of tropospheric ozone and related tracers: Description and evaluation of MOZART, version 2, J. Geophys. Res., 108, 4784, doi:10.1029/2002JD002853, 2003. 3632
Jacobson, M. Z.: Numerical Techniques to Solve Condesational and Dissolutional Growth Equations When Growth is Coupled to Reversible Reactions, Aerosol Sci. Technol., 27, 491–498, 1997a. 3630
Jacobson, M. Z.: Development and application of a new air pollution modeling system II. Aerosol module structure and design, Atmos. Environ., 31, 131–144, doi:10.1016/1352-2310(96)00202-6, 1997b. 3628
Jacobson, M. Z.: Global direct radiative forcing due to multicomponent anthropogenic and natural aerosols, J. Geophys. Res., 106, 1551–1568, 2001. 3625
Jacobson, M. Z.: Analysis of aerosol interactions with numerical techniques for solving coagulation, nucleation, condensation, dissolution and reversible chemistry among multiple size distributions, Aerosol Sci. Technol., 27, 491–498, 2002. 3630
Jacobson, M. Z.: Fundamentals of Atmospheric Modeling, 2nd Edn., Cambridge University Press, New York, 2005. 3630





GMDD
4, 3623–3690, 2011



Jathar, S. H., Farina, S. C., Robinson, A. L., and Adams, P. J.: The influence of semi-volatile and reactive primary emissions on the abundance and properties of global organic aerosol, Atmos. Chem. Phys., 11, 7727–7746, doi:10.5194/acp-11-7727-2011, 2011. 3642

Jennings, S., O'Dowd, C., O'Connor, T., and McGovern, F.: Physical characteristics of the ambient aerosol at mace head, Atmos. Environ., Part A. General Topics, 25, 557–562, doi:10.1016/0960-1686(91)90052-9, 1991. 3649

Jeuken, A. B. M., Siegmund, P. C., Heijboer, L. C., Feichter, J., and Bengtsson, L.: On the potential of assimilating meteorological analyses in a global climate model for the purpose of model validation, J. Geophys. Res., 101, 16939–16950, 1996. 3627

Jurányi, Z., Gysel, M., Weingartner, E., Bukowiecki, N., Kammermann, L., and Baltensperger, U.: A 17 month climatology of the cloud condensation nuclei number concentration at the high alpine site Jungfraujoch, J. Geophys. Res., 116, D10204, doi:10.1029/2010JD015199, 2011. 3649

Kazil, J., Stier, P., Zhang, K., Quaas, J., Kinne, S., O'Donnell, D., Rast, S., Esch, M., Ferrachat, S., Lohmann, U., and Feichter, J.: Aerosol nucleation and its role for clouds and Earth's radiative forcing in the aerosol-climate model ECHAM5-HAM, Atmos. Chem. Phys., 10, 10733–10752, doi:10.5194/acp-10-10733-2010, 2010. 3650

Kerkweg, A., Buchholz, J., Ganzeveld, L., Pozzer, A., Tost, H., and Jöckel, P.: Technical Note: An implementation of the dry removal processes DRY DEPosition and SEDImentation in the Modular Earth Submodel System (MESSy), Atmos. Chem. Phys., 6, 4617–4632, doi:10.5194/acp-6-4617-2006, 2006. 3635

Kerminen, V. and Kulmala, M.: Analytical formulae connecting the "real" and the "apparent" nucleation rate and the nuclei number concentration for atmospheric nucleation events, J. Aerosol Sci., 33, 609–622, 2002. 3631

Kinne, S., Lohmann, U., Feichter, J., Schulz, M., Timmreck, C., Ghan, S., Easter, R., Chin, M., Ginoux, P., Takemura, T., Tegen, I., Koch, D., Herzog, M., Penner, J., Pitari, G., Holben, B., Eck, T., Smirnov, A., Dubovik, O., Slutsker, I., Tanre, D., Torres, O., Mishchenko, M., Geogdzhayev, I., Chu, D. A., and Kaufman, Y.: Monthly averages of aerosol properties: A global comparison among models, satellite data, and AERONET ground data, J. Geophys. Res., 108, 4634, doi:10.1029/2004JD004999, 2003. 3675

Koch, D., Schulz, M., Kinne, S., McNaughton, C., Spackman, J. R., Balkanski, Y., Bauer, S., Berntsen, T., Bond, T. C., Boucher, O., Chin, M., Clarke, A., De Luca, N., Dentener, F., Diehl, T., Dubovik, O., Easter, R., Fahey, D. W., Feichter, J., Fillmore, D., Freitag, S., Ghan, S.,





GMDD
4, 3623–3690, 2011



Ginoux, P., Gong, S., Horowitz, L., Iversen, T., Kirkevåg, A., Klimont, Z., Kondo, Y., Krol, M., Liu, X., Miller, R., Montanaro, V., Moteki, N., Myhre, G., Penner, J. E., Perlwitz, J., Pitari, G., Reddy, S., Sahu, L., Sakamoto, H., Schuster, G., Schwarz, J. P., Seland, Ø., Stier, P., Takegawa, N., Takemura, T., Textor, C., van Aardenne, J. A., and Zhao, Y.: Evaluation of black carbon estimations in global aerosol models, Atmos. Chem. Phys., 9, 9001–9026, doi:10.5194/acp-9-9001-2009, 2009. 3655

Koepke, P., Hess, M., Schult, I., and Shettle, E.: Global Aerosol Data Set, Tech. rep., Max-Planck Institute for Meteorology, 1997. 3675

Kokkola, H., Korhonen, H., Lehtinen, K. E. J., Makkonen, R., Asmi, A., Järvenoja, S., Anttila, T., Partanen, A.-I., Kulmala, M., Järvinen, H., Laaksonen, A., and Kerminen, V.-M.: SALSA - a Sectional Aerosol module for Large Scale Applications, Atmos. Chem. Phys., 8, 2469–2483, doi:10.5194/acp-8-2469-2008, 2008. 3626, 3632, 3633

Korhonen, H., Carslaw, K. S., Spracklen, D. V., Ridley, D. A., and Ström, J.: A global model study of processes controlling aerosol size distributions in the Arctic spring and summer, J. Geophys. Res., 113, D08211, doi:10.1029/2007JD009114, 2008. 3655

Kulmala, M., Lehtinen, K. E. J., and Laaksonen, A.: Cluster activation theory as an explanation of the linear dependence between formation rate of 3 nm particles and sulphuric acid concentration, Atmos. Chem. Phys., 6, 787–793, doi:10.5194/acp-6-787-2006, 2006. 3630

Kulmala, M., Asmi, A., Lappalainen, H. K., Carslaw, K. S., Pöschl, U., Baltensperger, U., Hov, Ø., Brenquier, J.-L., Pandis, S. N., Facchini, M. C., Hansson, H.-C., Wiedensohler, A., and O'Dowd, C. D.: Introduction: European Integrated Project on Aerosol Cloud Climate and Air Quality interactions (EUCAARI) – integrating aerosol research from nano to global scales, Atmos. Chem. Phys., 9, 2825–2841, doi:10.5194/acp-9-2825-2009, 2009. 3649

Kulmala, M., Asmi, A., Lappalainen, H. K., Baltensperger, U., Brenguier, J.-L., Facchini, M. C., Hansson, H.-C., Hov, Ø., O'Dowd, C. D., Pöschl, U., Wiedensohler, A., Boers, R., Boucher, O., de Leeuw, G., Denier van den Gon, H., Feichter, J., Krejci, R., Laj, P., Lihavainen, H., Lohmann, U., McFiggans, G., Mentel, T., Pilinis, C., Riipinen, I., Schulz, M., Stohl, A., Swietlicki, E., Vignati, E., Amann, M., Amann, M., Alves, C., Arabas, S., Artaxo, P., Beddows, D. C. S., Bergström, R., Beukes, J. P., Bilde, M., Burkhart, J. F., Canonaco, F., Clegg, S., Coe, H., Crumeyrolle, S., D'Anna, B., Decesari, S., Gilardoni, S., Fischer, M., Fjæraa, A. M., Fountoukis, C., George, C., Gomes, L., Halloran, P., Hamburger, T., Harrison, R. M., Herrmann, H., Hoffmann, T., Hoose, C., Hu, M., H˜rrak, U., Iinuma, Y., Iversen, T., Josipovic, M., Kanakidou, M., Kiendler-Scharr, A., Kirkevåg, A., Kiss, G., Klimont, Z., Kolmonen, P., Komp-





GMDD
4, 3623–3690, 2011



pula, M., Kristjánsson, J.-E., Laakso, L., Laaksonen, A., Labonnote, L., Lanz, V. A., Lehtinen, K. E. J., Makkonen, R., McMeeking, G., Merikanto, J., Minikin, A., Mirme, S., Morgan, W. T., Nemitz, E., O'Donnell, D., Panwar, T. S., Pawlowska, H., Petzold, A., Pienaar, J. J., Pio, C., Plass-Duelmer, C., Prévôt, A. S. H., Pryor, S., Reddington, C. L., Roberts, G., Rosenfeld, D., Schwarz, J., Seland, Ø., Sellegri, K., Shen, X. J., Shiraiwa, M., Siebert, H., Sierau, B., Simpson, D., Sun, J. Y., Topping, D., Tunved, P., Vaattovaara, P., Vakkari, V., Veefkind, J. P., Visschedijk, A., Vuollekoski, H., Vuolo, R., Wehner, B., Wildt, J., Woodward, S., Worsnop, D. R., van Zadelhoff, G.-J., Zardini, A. A., Zhang, K., van Zyl, P. G., Kerminen, V.-M., S. Carslaw, K., and Pandis, S. N.: General overview: European Integrated project on Aerosol Cloud Climate and Air Quality interactions (EUCAARI) – integrating aerosol research from nano to global scales, Atmos. Chem. Phys. Discuss., 11, 17941–18160, doi:10.5194/acpd-11-17941-2011, 2011. 3649

Lehtinen, K., Rannik, U., Petäjä, T., Kulmala, M., and Hari, P.: Nucleation rate and vapor concentration estimations using a least-squares aerosol dynamics method, J. Geophys. Res. Atmos., 109, D21209, 10.1029/2004JD004893, 2004. 3630

Lehtinen, K. E., Maso, M. D., Kulmala, M., and Kerminen, V.-M.: Estimating nucleation rates from apparent particle formation rates and vice versa: Revised formulation of the Kerminen-Kulmala equation, J. Aerosol Sci., 38, 988–994, doi:10.1016/j.jaerosci.2007.06.009, 2007. 3631

Lesins, G., Chylek, P., and Lohmann, U.: A study of internal and external mixing scenarios and its effect on aerosol optical properties and direct radiative forcing, J. Geophys. Res., 107, 4094, doi:10.1029/2001JD000973, 2002. 3639

Levy, R. C., Remer, L. A., Kleidman, R. G., Mattoo, S., Ichoku, C., Kahn, R., and Eck, T. F.: Global evaluation of the Collection 5 MODIS dark-target aerosol products over land, Atmos. Chem. Phys., 10, 10399–10420, doi:10.5194/acp-10-10399-2010, 2010. 3653

Liao, H., Zhang, Y., Chen, W.-T., Raes, F., and Seinfeld, J. H.: Effect of chemistry-aerosol-climate coupling on predictions of future climate and future levels of tropospheric ozone and aerosols, J. Geophys. Res., 114, D10306, doi:10.1029/2008JD010984, 2009. 3626

Lihavainen, H., Kerminen, V.-M., Komppula, M., Hyvärinen, A.-P., Laakia, J., Saarikoski, S., Makkonen, U., Kivekäs, N., Hillamo, R., Kulmala, M., and Viisanen, Y.: Measurements of the relation between aerosol properties and microphysics and chemistry of low level liquid water clouds in Northern Finland, Atmos. Chem. Phys., 8, 6925–6938, doi:10.5194/acp-8-6925-2008, 2008. 3649





GMDD
4, 3623–3690, 2011



Lin, S.-J. and Rood, R. B.: Multidimensional Flux-Form Semi-Lagrangian Transport Schemes, MWR, 124, 2046–2070, doi:10.1175/1520-0493(1996)124%253C2046:MFFSLT%253E2.0.CO;2, 1996. 3627
Liu, C., Moncrieff, M. W., and Grabowski, W. W.: Hierarchial modelling of tropical convective systems using explicit and parametrized approaches, Q. J. R. Meteorol. Soc., 127, 493–515, 2001. 3640
Liu, H. Q., Pinker, R. T., and Holben, B. N.: A global view of aerosols from merged transport models, satellite, and ground observations, J. Geophys. Res., 110, D10S15, doi:10.1029/2004JD004695, 2005a. 3626
Liu, X., Penner, J. E., and Herzog, M.: Global modeling of aerosol dynamics: Model description, evaluation, and interactions between sulfate and nonsulfate aerosols, J. Geophys. Res., 110, D18206, doi:10.1029/2004JD005674, 2005b. 3641, 3642, 3643, 3644, 3645, 3656, 3676, 3677, 3678, 3679
Lohmann, U., Stier, P., Hoose, C., Ferrachat, S., Kloster, S., Roeckner, E., and Zhang, J.: Cloud microphysics and aerosol indirect effects in the global climate model ECHAM5-HAM, Atmos. Chem. Phys., 7, 3425–3446, doi:10.5194/acp-7-3425-2007, 2007. 3626
Mann, G. W., Carslaw, K. S., Spracklen, D. V., Ridley, D. A., Manktelow, P. T., Chipperfield, M. P., Pickering, S. J., and Johnson, C. E.: Description and evaluation of GLOMAP-mode: a modal global aerosol microphysics model for the UKCA composition-climate model, Geosci. Model Dev., 3, 519–551, doi:10.5194/gmd-3-519-2010, 2010. 3625
Martonchik, J., Diner, D. J., Kahn, R., Ackerman, T. P., Verstraete, M. M., and Pinty, B., and Gordon, H. R.: Techniques for the retrieval of aerosol properties over land and ocean using multi-angle imaging, IEEE Trans. Geosci. Rem. Sens., 36, 1212–1227, 1998. 3653
Mayol-Bracero, O. L., Guyon, P., Graham, B., Roberts, G., Andreae, M. O., Decesari, S., Facchini, M. C., Fuzzi, S., and Artaxo, P.: Water-soluble organic compounds in biomass burning aerosols over Amazonia 2. Apportionment of the chemical composition and importance of the polyacidic fraction, J. Geophys. Res., 107, 8091, doi:10.1029/2001JD000522, 2002. 3636
Mielonen, T., Levy, R. C., Aaltonen, V., Komppula, M., de Leeuw, G., Huttunen, J., Lihavainen, H., Kolmonen, P., Lehtinen, K. E. J., and Arola, A.: Evaluating the assumptions of surface reflectance and aerosol type selection within the MODIS aerosol retrieval over land: the problem of dust type selection, Atmos. Meas. Tech., 4, 201–214, doi:10.5194/amt-4-201-2011, 2011. 3655
Monahan, E. C., Spiel, D. E., and Davidson, K. L.: A model of marine aerosol generation via





GMDD
4, 3623–3690, 2011



whitecaps and wave disruption, in: Oceanic Whitecaps and Their Role in Air-Sea Exchange, edited by: Monahan, E. and Mac Niocaill, G., 167–174, D. Reidel, Norwell, Massachusetts, 1986. 3637, 3638

Myhre, G.: Consistency Between Satellite-Derived and Modeled Estimates of the Direct Aerosol Effect, Science, 325, 187–190, doi:10.1126/science.1174461, 2009. 3625

Nightingale, P. D., Malin, G., Law, C. S., Watson, A. J., Liss, P. S., Liddicoat, M. I., Boutin, J., and Upstill-Goddard, R. C.: In situ evaluation of air-sea gas exchange parameterizations using novel conservative and volatile tracers, Global Biogeochem. Cy., 14, 373–387, doi:10.1029/1999GB900091, 2000. 3637

O'Donnell, D., Tsigaridis, K., and Feichter, J.: Estimating the direct and indirect effects of secondary organic aerosols using ECHAM5-HAM, Atmos. Chem. Phys., 11, 8635–8659, doi:10.5194/acp-11-8635-2011, 2011. 3626

Partanen, A.-I., Kokkola, H., Romakkaniemi, S., Kerminen, V.-M., Lehtinen, K., Bergman, T., Arola, A., and Korhonen, H.: Direct and indirect effects of sea spray geoengineering and the role of injected particle size, J. Geophys. Res., in press, doi:10.1029/2011JD016428, 2011. 3626

Pham, M., Mueller, J. F., Brasseur, G., Granier, C., and Megie, C.: A three-dimensional study of the tropospheric sulfate cycle, J. Geophys. Res., 100, 26 061–26 092, doi:10.1029/95JD02095, 1995. 3637

Pinty, B., Taberner, M., Haemmerle, V. R., Paradise, S. R., Vermote, E., Verstraete, M. M., Gobron, N., and Widlowski, J.-L.: Global-Scale Comparison of MISR and MODIS Land Surface Albedos, J. Climate, 24, 732–749, doi:10.1175/2010JCLI3709.1, 2010. 3653

Pringle, K. J., Tost, H., Message, S., Steil, B., Giannadaki, D., Nenes, A., Fountoukis, C., Stier, P., Vignati, E., and Lelieveld, J.: Description and evaluation of GMXe: a new aerosol submodel for global simulations (v1), Geosci. Model Dev., 3, 391–412, doi:10.5194/gmd-3-391-2010, 2010. 3625

Quaas, J., Ming, Y., Menon, S., Takemura, T., Wang, M., Penner, J. E., Gettelman, A., Lohmann, U., Bellouin, N., Boucher, O., Sayer, A. M., Thomas, G. E., McComiskey, A., Feingold, G., Hoose, C., Kristjánsson, J. E., Liu, X., Balkanski, Y., Donner, L. J., Ginoux, P. A., Stier, P., Grandey, B., Feichter, J., Sednev, I., Bauer, S. E., Koch, D., Grainger, R. G., Kirkevåg, A., Iversen, T., Seland, Ø., Easter, R., Ghan, S. J., Rasch, P. J., Morrison, H., Lamarque, J.-F., Iacono, M. J., Kinne, S., and Schulz, M.: Aerosol indirect effects – general circulation model intercomparison and evaluation with satellite data, Atmos. Chem. Phys., 9, 8697–





GMDD
4, 3623–3690, 2011



8717, doi:10.5194/acp-9-8697-2009, 2009. 3625
Reddy, M. S., Boucher, O., Bellouin, N., Schulz, M., Balkanski, Y., Dufresne, J.-L., and Pham, M.: Estimates of global multicomponent aerosol optical depth and direct radiative perturbation in the Laboratoire de Météorologie Dynamique general circulation model, J. Geophys. Res., 110, D10S16, doi:10.1029/2004JD004757, 2005. 3626
Remer, L. A., Kaufman, Y. J., Tanré, D., Mattoo, S., Chu, D. A., Martins, J. V., Li, R. R., Ichoku, C., Levy, R. C., Kleidman, R. G., Eck, T. F., Vermote, E., and Holben, B. N.: The MODIS Aerosol Algorithm, Products, and Validation, J. Atmos. Sci., 62, 947–973, doi:10.1175/JAS3385.1, 2005. 3653
Riipinen, I., Sihto, S.-L., Kulmala, M., Arnold, F., Dal Maso, M., Birmili, W., Saarnio, K., Teinilä, K., Kerminen, V.-M., Laaksonen, A., and Lehtinen, K. E. J.: Connections between atmospheric sulphuric acid and new particle formation during QUEST IIIIV campaigns in Heidelberg and Hyytiälä, Atmos. Chem. Phys., 7, 1899–1914, doi:10.5194/acp-7-1899-2007, 2007. 3630
Riipinen, I., Pierce, J. R., Yli-Juuti, T., Nieminen, T., Häkkinen, S., Ehn, M., Junninen, H., Lehtipalo, K., Petäjä, T., Slowik, J., Chang, R., Shantz, N. C., Abbatt, J., Leaitch, W. R., Kerminen, V.-M., Worsnop, D. R., Pandis, S. N., Donahue, N. M., and Kulmala, M.: Organic condensation: a vital link connecting aerosol formation to cloud condensation nuclei (CCN) concentrations, Atmos. Chem. Phys., 11, 3865–3878, doi:10.5194/acp-11-3865-2011, 2011. 3651
Roeckner, E., Bäuml, R., Bonaventura, L., Brokopf, R., Esch, M., Giorgetta, M., Hagemann, S., Kirchner, I., Kornblueh, L., Manzini, E., Rhodin, A., Schlese, U., Schulzweida, U., and Tompkins, A.: The atmospheric general circulation model ECHAM5, Part I: Model description, Tech. rep., Max-Planck Institute for Meteorology, Hamburg, Germany, 2003. 3627
Roeckner, E., Brokopf, R., Esch, M., Giorgetta, M., Hagemann, S., Kornblueh, L., Manzini, E., Schlese, U., and Schulzweida, U.: The atmospheric general circulation model ECHAM5, Part II: Sensitivity of simulated climate to horizontal and vertical resolution, Tech. rep., Max-Planck Institute for Meteorology, Hamburg, Germany, 2004. 3627
Schwartz, S. E., Charlson, R. J., Kahn, R. A., Ogren, J. A., and Rodhe, H.: Why Hasn't Earth Warmed as Much as Expected?, J. Climate, 23, 2453–2464, doi:10.1175/2009JCLI3461.1, 2010. 3625
Seinfeld, J. and Pandis, S.: Atmospheric chemistry and physics: From air pollution to climate change, 2nd Edn., Wiley Interscience, 2006. 3629, 3633, 3634, 3635





GMDD
4, 3623–3690, 2011



Sesartic, A., Lohmann, U., and Storelvmo, T.: Bacteria in the ECHAM5-HAM global climate model, Atmos. Chem. Phys. Discuss., 11, 1457–1488, doi:10.5194/acpd-11-1457-2011, 2011. 3626

Shettle, E. P. and Fenn, R.: Models of the aerosols of the lower atmosphere and the effects of humidity variations on their optical properties, Tech. rep., Air Force Geoph. Lab., Massachusetts, 1979. 3675

Shi, Y., Zhang, J., Reid, J. S., Holben, B., Hyer, E. J., and Curtis, C.: An analysis of the collection 5 MODIS over-ocean aerosol optical depth product for its implication in aerosol assimilation, Atmos. Chem. Phys., 11, 557–565, doi:10.5194/acp-11-557-2011, 2011. 3654

Shindell, D. T., Chin, M., Dentener, F., Doherty, R. M., Faluvegi, G., Fiore, A. M., Hess, P., Koch, D. M., MacKenzie, I. A., Sanderson, M. G., Schultz, M. G., Schulz, M., Stevenson, D. S., Teich, H., Textor, C., Wild, O., Bergmann, D. J., Bey, I., Bian, H., Cuvelier, C., Duncan, B. N., Folberth, G., Horowitz, L. W., Jonson, J., Kaminski, J. W., Marmer, E., Park, R., Pringle, K. J., Schroeder, S., Szopa, S., Takemura, T., Zeng, G., Keating, T. J., and Zuber, A.: A multi-model assessment of pollution transport to the Arctic, Atmos. Chem. Phys., 8, 5353–5372, doi:10.5194/acp-8-5353-2008, 2008. 3655

Sihto, S.-L., Kulmala, M., Kerminen, V.-M., Dal Maso, M., Petäjä, T., Riipinen, I., Korhonen, H., Arnold, F., Janson, R., Boy, M., Laaksonen, A., and Lehtinen, K. E. J.: Atmospheric sulphuric acid and aerosol formation: implications from atmospheric measurements for nucleation and early growth mechanisms, Atmos. Chem. Phys., 6, 4079–4091, doi:10.5194/acp-6-4079-2006, 2006. 3630

Sihto, S.-L., Mikkilä, J., Vanhanen, J., Ehn, M., Liao, L., Lehtipalo, K., Aalto, P. P., Duplissy, J., Petäjä, T., Kerminen, V.-M., Boy, M., and Kulmala, M.: Seasonal variation of CCN concentrations and aerosol activation properties in boreal forest, Atmos. Chem. Phys. Discuss., 10, 28231–28272, doi:10.5194/acpd-10-28231-2010, 2010. 3651

Smith, M. and Harrison, N.: The sea spray generation function, J/ Aerosol Sci., proceedings of the 1998 International Aerosol Conference Part 1, 29, S189–S190, doi:10.1016/S0021-8502(98)00280-8, 1998. 3637

Spracklen, D. V., Pringle, K. J., Carslaw, K. S., Chipperfield, M. P., and Mann, G. W.: A global off-line model of size-resolved aerosol microphysics: I. Model development and prediction of aerosol properties, Atmos. Chem. Phys., 5, 2227–2252, doi:10.5194/acp-5-2227-2005, 2005. 3625

Spracklen, D. V., Carslaw, K. S., Merikanto, J., Mann, G. W., Reddington, C. L., Pickering, S.,





GMDD

4, 3623–3690, 2011



Ogren, J. A., Andrews, E., Baltensperger, U., Weingartner, E., Boy, M., Kulmala, M., Laakso, L., Lihavainen, H., Kivekäs, N., Komppula, M., Mihalopoulos, N., Kouvarakis, G., Jennings, S. G., O'Dowd, C., Birmili, W., Wiedensohler, A., Weller, R., Gras, J., Laj, P., Sellegri, K., Bonn, B., Krejci, R., Laaksonen, A., Hamed, A., Minikin, A., Harrison, R. M., Talbot, R., and Sun, J.: Explaining global surface aerosol number concentrations in terms of primary emissions and particle formation, Atmos. Chem. Phys., 10, 4775–4793, doi:10.5194/acp-10-4775-2010, 2010. 3650

Stier, P., Feichter, J., Kinne, S., Kloster, S., Vignati, E., Wilson, J., Ganzeveld, L., Tegen, I., Werner, M., Balkanski, Y., Schulz, M., Boucher, O., Minikin, A., and Petzold, A.: The aerosol-climate model ECHAM5-HAM, Atmos. Chem. Phys., 5, 1125–1156, doi:10.5194/acp-5-1125-2005, 2005. 3625, 3626, 3627, 3633, 3634, 3635, 3636, 3637

Stokes, R. and Robinson, R. A.: Interactions in aqueous nonelectrolytes solutions, I, Solute-solvent equilibria, J. Phys. Chem., 70, 2131 doi:10.1021/j100879a010, 1966. 3630

Tegen, I., Harrison, S. P., Kohfeld, K., Prentice, I. C.and Coe, M., and Heimann, M.: Impact of vegetation and preferential source areas on global dust aerosol: Results from a model study, J. Geophys. Res., 107, 4576, doi:10.1029/2001JD000963, 2002. 3639

Textor, C., Schulz, M., Guibert, S., Kinne, S., Balkanski, Y., Bauer, S., Berntsen, T., Berglen, T., Boucher, O., Chin, M., Dentener, F., Diehl, T., Easter, R., Feichter, H., Fillmore, D., Ghan, S., Ginoux, P., Gong, S., Grini, A., Hendricks, J., Horowitz, L., Huang, P., Isaksen, I., Iversen, I., Kloster, S., Koch, D., Kirkevåg, A., Kristjansson, J. E., Krol, M., Lauer, A., Lamarque, J. F., Liu, X., Montanaro, V., Myhre, G., Penner, J., Pitari, G., Reddy, S., Seland, Ø., Stier, P., Takemura, T., and Tie, X.: Analysis and quantification of the diversities of aerosol life cycles within AeroCom, Atmos. Chem. Phys., 6, 1777–1813, doi:10.5194/acp-6-1777-2006, 2006. 3640, 3644, 3645, 3656, 3676, 3677, 3678, 3679

Timmreck, C. and Schulz, M.: Significant dust simulation differences in nudged and climatological operation mode of the AGCM ECHAM, J. Geophys. Res., 109, D13202, doi:10.1029/2003JD004381, 2004. 3628

Toon, O. B. and Ackerman, T. P.: Algorithms for the calculation of scattering by stratified spheres, Appl. Optics, 20, 3657–3660, 1981. 3639

Tunved, P., Ström, J., and Hansson, H.-C.: An investigation of processes controlling the evolution of the boundary layer aerosol size distribution properties at the Swedish background station Aspvreten, Atmos. Chem. Phys., 4, 2581–2592, doi:10.5194/acp-4-2581-2004, 2004. 3649





GMDD
4, 3623–3690, 2011



Uppala, S. M., Kållberg, P. W., Simmons, A. J., Andrae, U., Bechtold, V. D. C., Fiorino, M., Gibson, J. K., Haseler, J., Hernandez, A., Kelly, G. A., Li, X., Onogi, K., Saarinen, S., Sokka, N., Allan, R. P., Andersson, E., Arpe, K., Balmaseda, M. A., Beljaars, A. C. M., Berg, L. V. D., Bidlot, J., Bormann, N., Caires, S., Chevallier, F., Dethof, A., Dragosavac, M., Fisher, M., Fuentes, M., Hagemann, S., Hólm, E., Hoskins, B. J., Isaksen, L., Janssen, P. A. E. M., Jenne, R., Mcnally, A. P., Mahfouf, J.-F., Morcrette, J.-J., Rayner, N. A., Saunders, R. W., Simon, P., Sterl, A., Trenberth, K. E., Untch, A., Vasiljevic, D., Viterbo, P., and Woollen, J.: The ERA-40 re-analysis, Quart. J. Roy. Meteorol. Soc., 131, 2961–3012, doi:10.1256/qj.04.176, 2005. 3628

Vehkamäki, H., Kulmala, M., Napari, I., Lehtinen, K. E. J., Timmreck, C., Noppel, M., and Laaksonen, A.: An improved parameterization for sulfuric acid/water nucleation rates for tropospheric and stratospheric conditions, J. Geophys. Res., 107, 4622–4631, 2002. 3630, 3631

Vignati, E., Wilson, J., and Stier, P.: M7: An efficient size-resolved aerosol microphysics module for large-scale aerosol transport models, J. Geophys. Res., 109, D22202, doi:10.1029/2003JD004485, 2004. 3625, 3627, 3632

Yuan, X.: High-wind-speed evaluation in the Southern Ocean, J. Geophys. Res., 109, D13101, doi:10.1029/2003JD004179, 2004. 3645

Zhang, K., Wan, H., Wang, B., Zhang, M., Feichter, J., and Liu, X.: Tropospheric aerosol size distributions simulated by three online global aerosol models using the M7 microphysics module, Atmos. Chem. Phys., 10, 6409–6434, doi:10.5194/acp-10-6409-2010, 2010. 3625

Zhang, Y., Seigneur, C., Seinfeld, J. H., Jacobson, M. Z., and Binkowski, F. S.: Simulation of Aerosol Dynamics: A Comparative Review of Algorithms Used in Air Quality Models, Aerosol Sci. Technol., 31, 487–514, doi:10.1080/027868299304039, 1999. 3626





GMDD
4, 3623–3690, 2011



**Table 1.** Particle diameter limits within all sections in SALSA. Please note that the limits in parallel size bins are the same.

| Bin | Solubility | Minimum diameter | maximum diameter |
|---|---|---|---|
| 1a1 | soluble | 3.00 nm | 7.7 nm |
| 1a2 | soluble | 7.7 nm | 19.6 nm |
| 1a3 | soluble | 19.6 nm | 50.0 nm |
| 2a1 | soluble | 50.0 nm | 96.7 nm |
| 2a2 | soluble | 96.7 nm | 187.0 nm |
| 2a3 | soluble | 187 nm | 362.0 nm |
| 2a4 | soluble | 362 nm | 700.0 nm |
| 2b1 | insoluble | 50.0 nm | 96.7 nm |
| 2b2 | insoluble | 96.7 nm | 187.0 nm |
| 2b3 | insoluble | 187.0 nm | 362.0 nm |
| 2b4 | insoluble | 362.0 nm | 700.0 nm |
| 3a1 | soluble | 0.70 µm | 1.70 µm |
| 3a2 | soluble | 1.70 µm | 4.12 µm |
| 3a3 | soluble | 4.12 µm | 1.00 µm |
| 3b1 | insoluble | 0.70 µm | 1.70 µm |
| 3b2 | insoluble | 1.70 µm | 4.12 µm |
| 3b3 | insoluble | 4.12 µm | 1.00 µm |
| 3c1 | insoluble | 0.70 µm | 1.70 µm |
| 3c2 | insoluble | 1.70 µm | 4.12 µm |
| 3c3 | insoluble | 4.12 µm | 1.00 µm |





GMDD
4, 3623–3690, 2011



**Table 2.** The processes have been limited to a certain size ranges. Coagulation of large particles is not considered due to low importance. Dry deposition and sedimentation have very limited effect on the population in the smaller soluble size ranges. Nucleation only creates new particles in the smallest size section.

| Process | 1a | 2a | 2b | 3a | 3b | 3c |
|---|---|---|---|---|---|---|
| Nucleation | o | | | | | |
| Condensation | o | o | o | o | o | o |
| Coagulation | o | o | o | | | |
| Wet deposition | o | o | o | o | o | o |
| Dry deposition | | | o | o | o | o |
| Sedimentation | | | o | o | o | o |





GMDD
4, 3623–3690, 2011





**Table 3.** Compound distribution in the three subranges. Characters a-c after subrange indicator refer to parallel subranges, a for soluble subrange, b for insoluble and c for cloud activating insoluble subrange. In subrange 3 the number tracer is assumed to consist solely seasalt or dust (marked with [∘]).

| | Abbrev. | 1a | 2a | 2b | 3a | 3b | 3c |
|---|---|---|---|---|---|---|---|
| Sulphate | SU | ∘ | ∘ | ∘ | | | |
| Organic carbon | OC | ∘ | ∘ | ∘ | | | |
| Black carbon | BC | | ∘ | ∘ | | | |
| Sea salt | SS | | ∘ | | [∘] | | |
| Dust | DU | | ∘ | ∘ | | [∘] | [∘] |
| Water soluble | WS | | | | | | ∘ |





GMDD
4, 3623–3690, 2011



**Table 4.** Cloud scavenging parameter $R_i$ for the subranges of SALSA. The coefficients remain the same for whole subrange with an exception with smallest size section 1a1 where the parameter has been defined separately as it is the only bin within the size range of nucleation mode of M7.

| Subrange | Stratiform Liquid | Stratiform Mixed | Stratiform Ice | Convective Mixed |
|---|---|---|---|---|
| 1a1 | 0.10 | 0.10 | 0.10 | 0.20 |
| 1a | 0.25 | 0.40 | 0.10 | 0.60 |
| 2a | 0.85 | 0.75 | 0.10 | 0.99 |
| 2b | 0.20 | 0.10 | 0.10 | 0.20 |
| 3a | 0.99 | 0.75 | 0.10 | 0.99 |
| 3b | 0.40 | 0.40 | 0.10 | 0.40 |
| 3c | 0.40 | 0.40 | 0.10 | 0.40 |





GMDD
4, 3623–3690, 2011



**Table 5.** Complex refractive indices by compound at $\lambda = 550$ nm.

| Species | Refractive index | Reference |
|---|---|---|
| Black Carbon | $1.85 + 7.1 \times 10^{-1}$ | Hess et al. (1998) |
| Organic | $1.53 + 5.5 \times 10^{-3}$ | Hess et al. (1998) |
| Sulphate | $1.43 + 1.0 \times 10^{-8}$ | Koepke et al. (1997) |
| Sea salt | $1.49 + 1.0 \times 10^{-8}$ | Shettle and Fenn (1979) |
| Dust | $1.52 + 1.1 \times 10^{-3}$ | Kinne et al. (2003) |
| Water | $1.33 + 2.0 \times 10^{-7}$ | Downing and Williams (1975) |





GMDD
4, 3623–3690, 2011



**Table 6.** Annual mean global sulphur cycle calculated using SALSA and M7 as well as results found in the literature. Additionally the simulated annual mean cover of low (1013–750 hPa), middle (740–460 hPa) and high (440–50 hPa) clouds is included.

| | SALSA | M7 | Liu et al. (2005b) | AeroCom (Textor et al., 2006) |
|---|---|---|---|---|
| $SO_4$ particle phase | | | | |
| Burden (Tg S) | 0.64 | 0.64 | 0.53–1.07 | 0.66 |
| Sources (Tg S $yr^{-1}$) | | | | |
| Total | 69.23 | 79.59 | | 59.67 |
| Emissions | 1.77 | 1.77 | 0.0–3.5 | |
| Condensation | 23.40 | 22.78 | | |
| Nucleation | 0.60 | 0.16 | | |
| Aqueous oxidation | 43.47 | 54.88 | 24.5–57.8 | |
| Sinks (Tg S $yr^{-1}$) | 60.92 | 77.95 | | |
| Wet Deposition | 59.46 | 75.38 | 34.7–61.0 | 53.0 |
| Dry Deposition | 1.47 | 2.42 | 3.9–18.0 | 7.23 |
| Sedimentation | 0.002 | 0.15 | | |
| Lifetime (days) | 3.61 | 2.92 | | 4.12 |
| $H_2SO_4$ gas phase | | | | |
| Burden (Tg S) | 0.0007 | 0.0009 | | |
| Sources (Tg S $yr^{-1}$) | | | | |
| Total | 27.88 | 23.06 | | |
| $SO_2$ + OH | 25.47 | 20.41 | | |
| DMS + OH | 2.41 | 2.65 | | |
| Sinks (Tg S $yr^{-1}$) | | | | |
| Total | 24.07 | 23.01 | | |
| Wet Deposition | 0.064 | 0.048 | | |
| Dry Deposition | 0.017 | 0.024 | | |
| Condensation | 23.40 | 22.78 | | |
| Nucleation | 0.60 | 0.16 | | |
| Lifetime (minutes) | 14.11 | 20.16 | | |





GMDD
4, 3623–3690, 2011



**Table 6.** Continued.

| | SALSA | M7 | Liu et al. (2005b) | AeroCom (Textor et al., 2006) |
|---|---|---|---|---|
| $SO_2$ | | | | |
| Burden (Tg S) | 0.64 | 0.87 | 0.20–0.61 | |
| Sources (Tg S $yr^{-1}$) | | | | |
| Total | 92.10 | 94.75 | | |
| Emissions | 71.03 | 71.03 | | |
| DMS + $NO_3$ | 4.86 | 5.39 | | |
| DMS + OH | 16.21 | 18.34 | | |
| Sinks (Tg S $yr^{-1}$) | | | | |
| Total | 89.98 | 93.22 | | |
| Wet Deposition | 3.66 | 2.62 | 0.0–19.9 | |
| Dry Deposition | 17.38 | 15.32 | 16.0–55.0 | |
| $SO_2$ + OH | 25.47 | 20.41 | 6.1–16.8 | |
| Aqueous oxidation | 43.47 | 54.88 | 24.5–57.8 | |
| Lifetime (days) | 2.55 | 1.96 | 0.6–2.6 | |
| DMS | | | | |
| Burden (Tg S) | 0.08 | 0.09 | 0.02–3.0 | |
| Sources (Tg S $yr^{-1}$) | | | | |
| Total | 23.46 | 26.37 | 10.7–23.7 | |
| Sinks (Tg S $yr^{-1}$) | | | | |
| Total | 23.48 | 26.38 | | |
| DMS + $NO_3$ | 4.86 | 5.39 | | |
| DMS + OH | 18.62 | 21.00 | | |
| Lifetime (days) | 1.21 | 1.21 | 0.5–3.0 | |
| Cloud cover | | | | |
| Low clouds | 0.17 | 0.19 | | |
| Mid clouds | 0.17 | 0.15 | | |
| High clouds | 0.24 | 0.24 | | |





GMDD
4, 3623–3690, 2011



**Table 7.** Annual mean global black carbon, organic carbon, sea salt and dust budgets calculated using SALSA and M7 together with budgets found in the literature. For Liu and AeroCom sedimentation is included in dry deposition).

| | SALSA | M7 | Liu et al. (2005b) | AeroCom multimodel mean (Textor et al., 2006) |
|---|---|---|---|---|
| Black carbon | | | | |
| Burden (Tg) | 0.07 | 0.10 | 0.12–0.29 | 0.24 |
| Sources (Tg $yr^{-1}$) | | | | |
| Emissions | 7.71 | 7.71 | | 11.90 |
| Sinks (Tg $yr^{-1}$) | 3.56 | 7.77 | | 13.14 |
| Wet deposition | 3.08 | 7.14 | 7.8–13.7 | 10.51 |
| Dry deposition | 0.47 | 0.61 | 1.6–4.6 | 2.63 |
| Sedimentation | 0.008 | 0.02 | | |
| Lifetime (days) | 3.84 | 4.96 | 3.3–8.4 | 7.12 |
| Organic carbon | | | | |
| Burden (Tg) | 0.96 | 0.93 | 0.95–1.8 | 1.70 |
| Sources (Tg $yr^{-1}$) | | | | |
| Emissions | 66.13 | 66.13 | | 96.60 |
| Sinks (Tg $yr^{-1}$) | 54.58 | 66.32 | | 105.49 |
| Wet | 49.88 | 61.16 | | 86.87 |
| Dry Deposition | 4.66 | 4.97 | | 18.62 |
| Sedimentation | 0.044 | 0.19 | | |
| Lifetime (days) | 5.30 | 5.14 | 3.9–8.4 | 6.54 |
| Sea salt | | | | |
| Burden (Tg) | 11.73 | 12.56 | 3.41–12.0 | 7.52 |
| Sources (Tg $yr^{-1}$) | | | | |
| Emissions | 7429.2 | 6234.8 | 1010–8076 | 16 600.00 |
| Sinks (Tg $yr^{-1}$) | 7446.5 | 6277.3 | | 13915 |
| Wet Deposition | 3054.6 | 3330.8 | | 2168 |
| Dry Deposition | 1693.4 | 1328.0 | | 11 747 |
| Sedimentation | 2698.5 | 1618.5 | | |
| Lifetime (days) | 0.58 | 0.74 | 0.19–0.99 | 0.48 |





GMDD
4, 3623–3690, 2011



**Table 7.** Continued.

| | SALSA | M7 | Liu et al. (2005b) | AeroCom multimodel mean (Textor et al., 2006) |
|---|---|---|---|---|
| Dust | | | | |
| Burden (Tg) | 13.11 | 19.3 | 4.3–35.9 | 19.20 |
| Sources (Tg yr$^{-1}$) | | | | |
| Emissions | 720.4 | 1603.4 | 820–5102 | 1840.0 |
| Sinks (Tg yr$^{-1}$) | 937.7 | 1649.3 | | 2172.48 |
| Wet Deposition | 439.9 | 961.8 | 486–4080 | 560.64 |
| Dry Deposition | 106.4 | 116.3 | 183–1027 | 1611.84 |
| Sedimentation | 391.5 | 517.1 | | |
| Lifetime (days) | 6.64 | 4.39 | 1.9–7.1 | 4.14 |
| Water soluble fraction in 3c | | | | |
| Burden (Tg) | 0.0087 | N/A | | |
| Sources (Tg yr$^{-1}$) | | | | |
| Emissions | N/A | | | |
| Sinks (Tg yr$^{-1}$) | 0.32 | | | |
| Wet Deposition | 0.26 | | | |
| Dry Deposition | 0.016 | | | |
| Sedimentation | 0.046 | | | |
| Lifetime (days) | | | | |





GMDD
4, 3623–3690, 2011



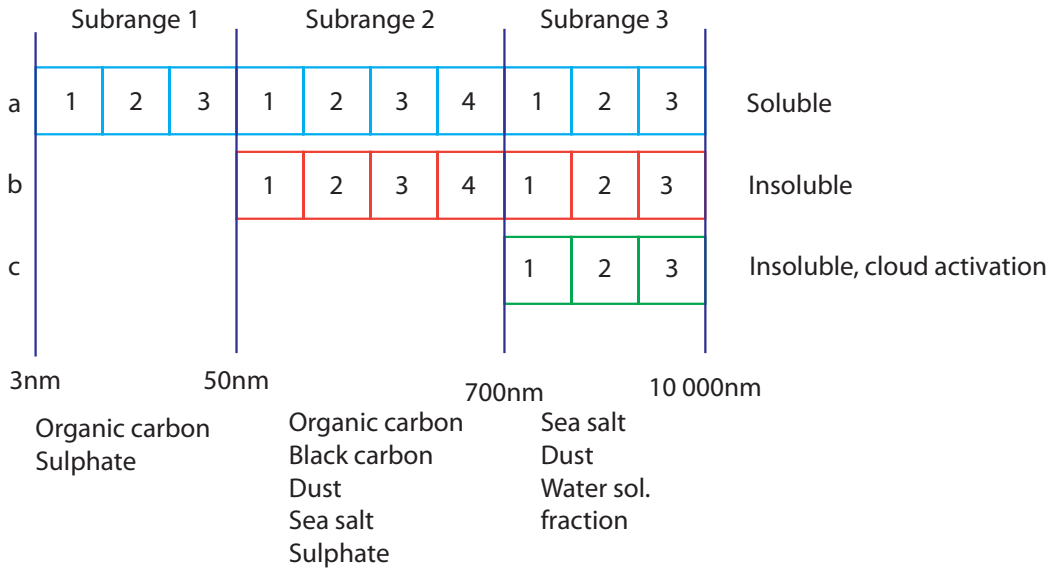


**Fig. 1.** Schematic of the SALSA sectional structure. There are three parallel sections a, b and c in three subranges each consisting of three or four sections. Parallel size sections in subclass a are soluble, in subclass b insoluble and in subclass c insoluble with possibility for soluble coating enabling cloud activation.





GMDD
4, 3623–3690, 2011



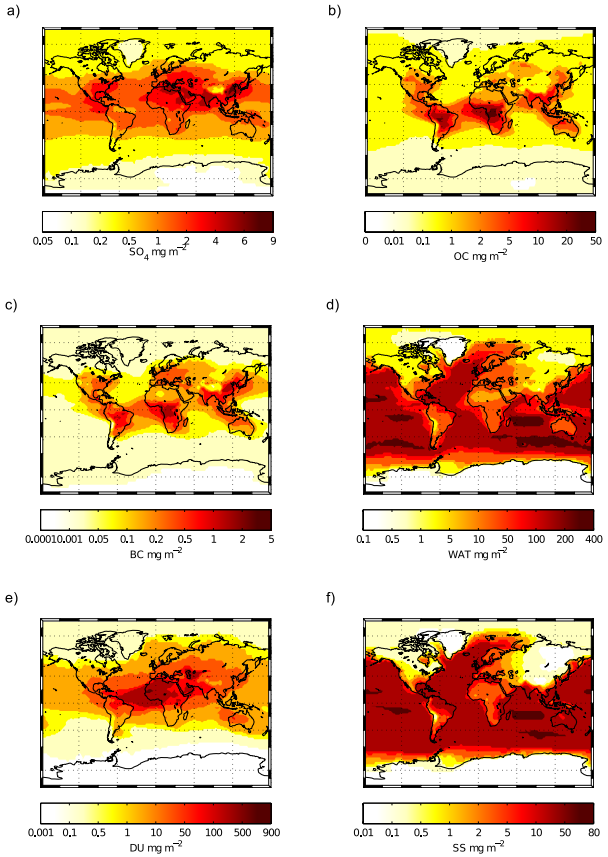


**Fig. 2.** Annual mean of vertically integrated column mass for year 2008 for **(a)** sulphate ($SO_4$), **(b)** organic carbon (OC), **(c)** black carbon (BC), **(d)** particulate water (WAT), **(e)** dust (DU) and **(f)** sea salt (SS) simulated with SALSA. All units are $mg\,m^{-2}$.





GMDD
4, 3623–3690, 2011

SALSA implementation in ECHAM5-HAM

T. Bergman et al.



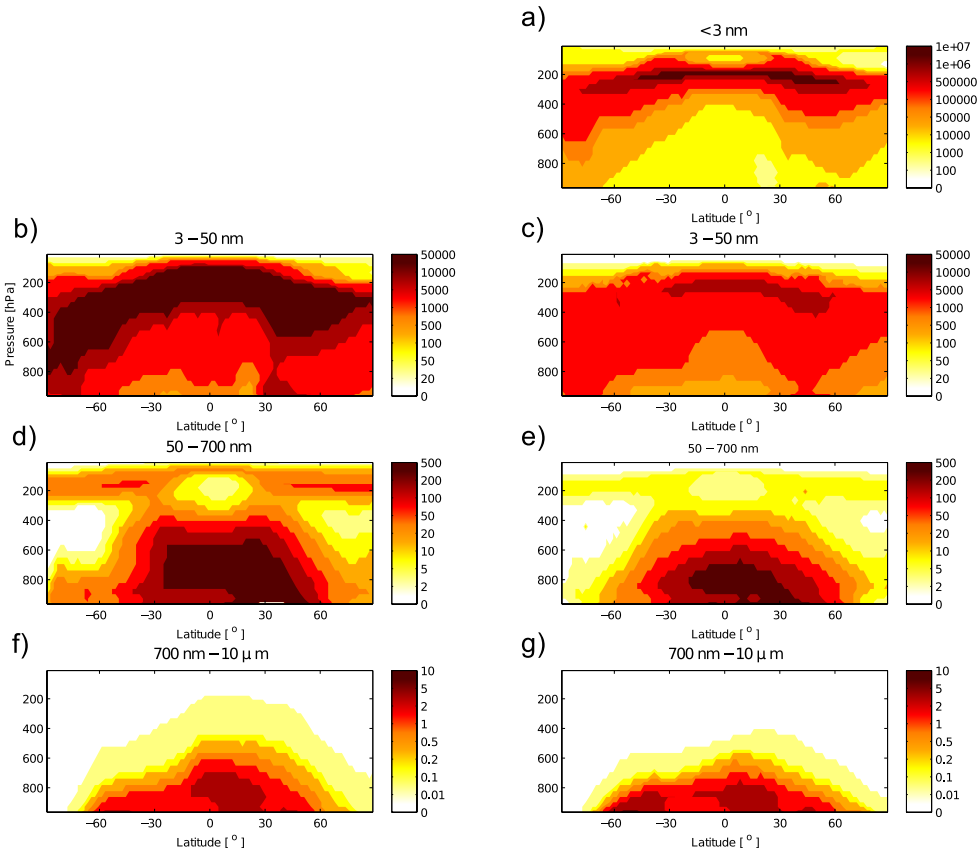


**Fig. 3.** Annual means of zonally averaged global vertical concentration distribution of particles. Left hand panels show concentrations with SALSA and right hand panels show the M7 concentrations mapped to SALSA subrange structure. Each panel corresponds to one subrange of SALSA: from the top 1,2,3. For M7 the top most panel shows particle concentrations below the 3 nm lower limit of SALSA.





GMDD
4, 3623–3690, 2011

SALSA implementation in ECHAM5-HAM

T. Bergman et al.



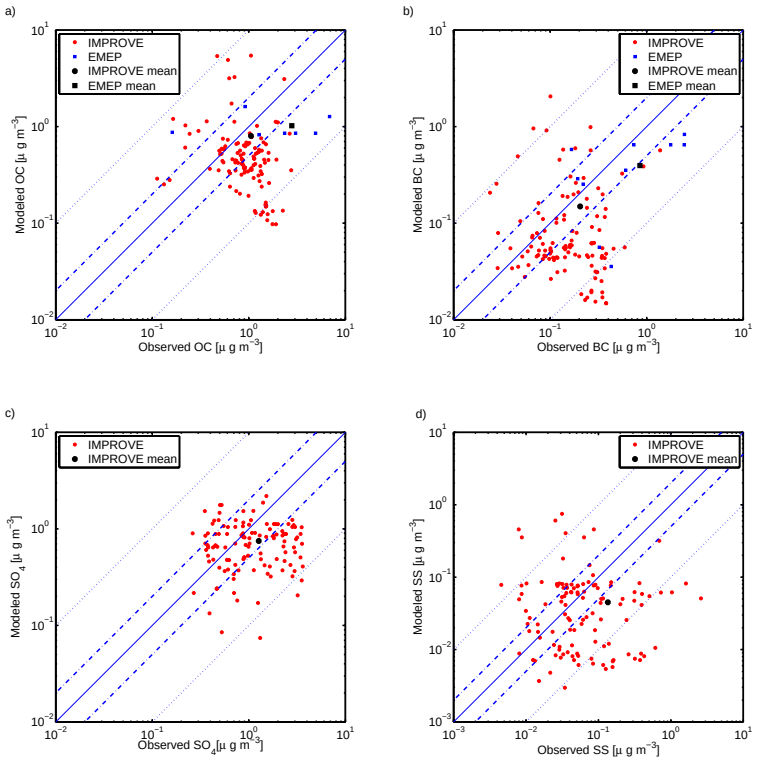


**Fig. 4.** Scatterplot of simulated and observed annual mean surface concentrations of organic carbon, black carbon, sulphate and sea salt. Red circles indicate comparison with IMPROVE network and blue squares represent EMEP network. Black symbols represent mean values of respective symbols. Solid line indicates 1:1 ratio between observations and simulated values. Similarly dot-dashed line indicates 1:2 and 2:1 ratios, and dotted lines indicate 1:10 and 10:1 ratios.





GMDD
4, 3623–3690, 2011



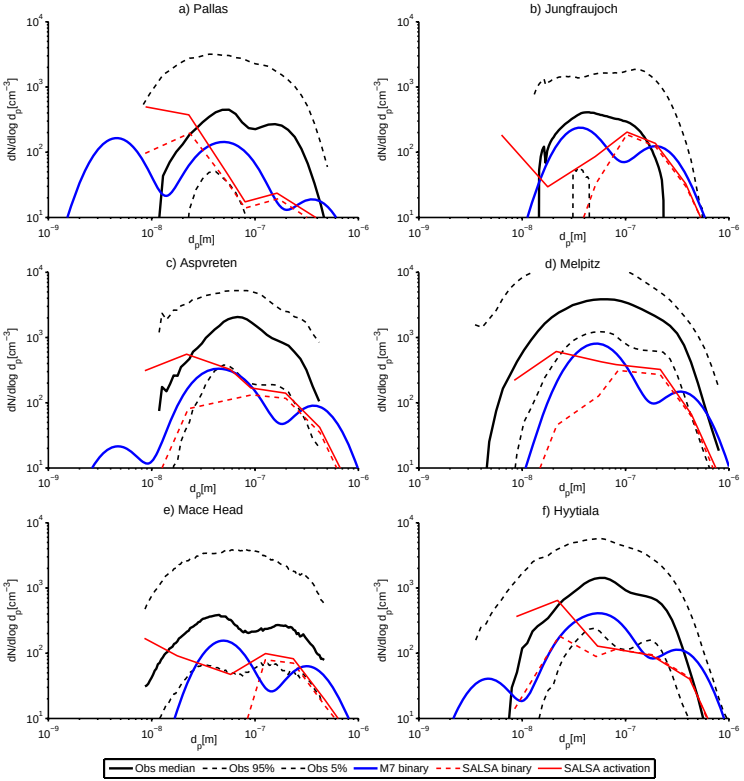


**Fig. 5.** Observed and simulated annual median size distributions for six measurement stations **(a)** Pallas, **(b)** Jungfraujoch, **(c)** Aspvreten, **(d)** Melpitz, **(e)** Mace Head and **(f)** Hyytiälä. Simulated size distribution for M7 is plotted in blue solid line. Simulated size distributions for SALSA are plotted with red solid line indicating activation type nucleation and with red dashed line for binary nucleation. Observed annual median size distributions are plotted in black, with dashed black lines showing the 95th and 5th percentiles of observed concentrations (Asmi et al., 2011).





GMDD
4, 3623–3690, 2011

SALSA implementation in ECHAM5-HAM

T. Bergman et al.



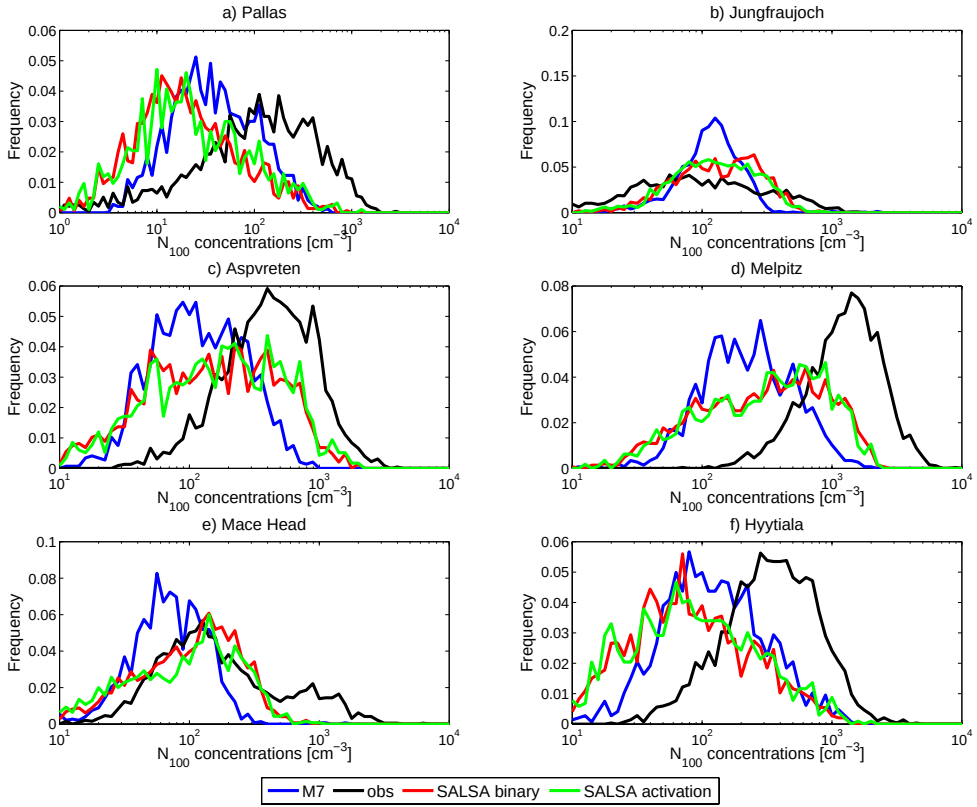


**Fig. 6.** Histograms of $N_{100}$ concentrations at six EUCAARI stations. The concentration bins are evenly distributed in the logarithmic concentration axes. Y-axis shows the relative fraction of each bin compared to total number of valid measurements.





GMDD
4, 3623–3690, 2011

SALSA implementation in ECHAM5-HAM

T. Bergman et al.



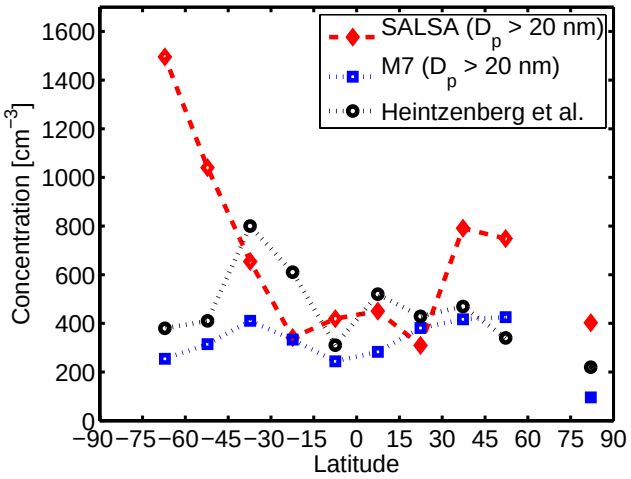


**Fig. 7.** Total annual mean sea surface concentration of particles in 10 latitude bands. Observed size distributions are marked with black, SALSA with red diamonds and M7 in blue squares. The observed mean values for the latitude bands are shown in black circles. As the observations have a lower cutoff diameter of 20 nm the modeled concentrations are shown only for particles larger than 20 nm in diameter.





GMDD
4, 3623–3690, 2011



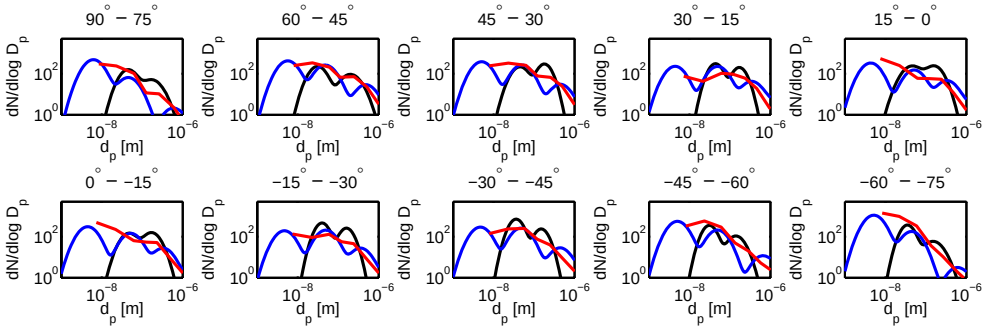


**Fig. 8.** Annual mean surface size distributions on 12 15° latitude bands for SALSA (red), M7 (blue) and observations (black) collected by Heintzenberg et al. (2000). Model size distributions have been calculated in the grid points corresponding to the locations of the observations.





GMDD
4, 3623–3690, 2011

SALSA implementation in ECHAM5-HAM

T. Bergman et al.



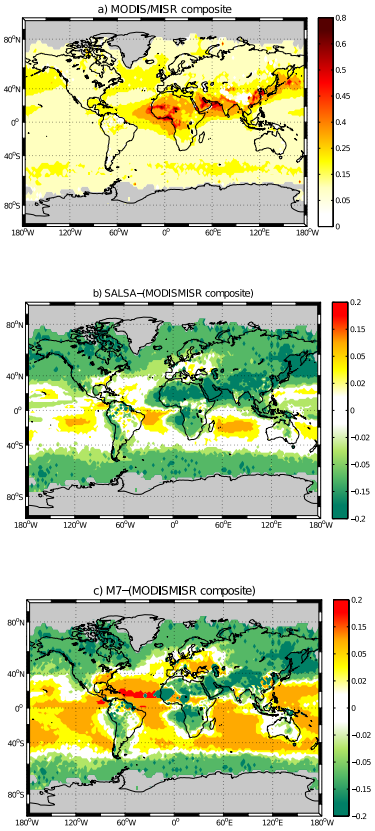


**Fig. 9.** Composite of retrieved annual mean of aerosol optical depth composite of MODIS and MISR **(a)**. The difference of AODs between MODIS/MISR composite and SALSA **(b)** and M7 **(c)**. Negative values indicate higher AOD with MODIS/MISR composite. Areas with no data are marked with gray.





GMDD
4, 3623–3690, 2011



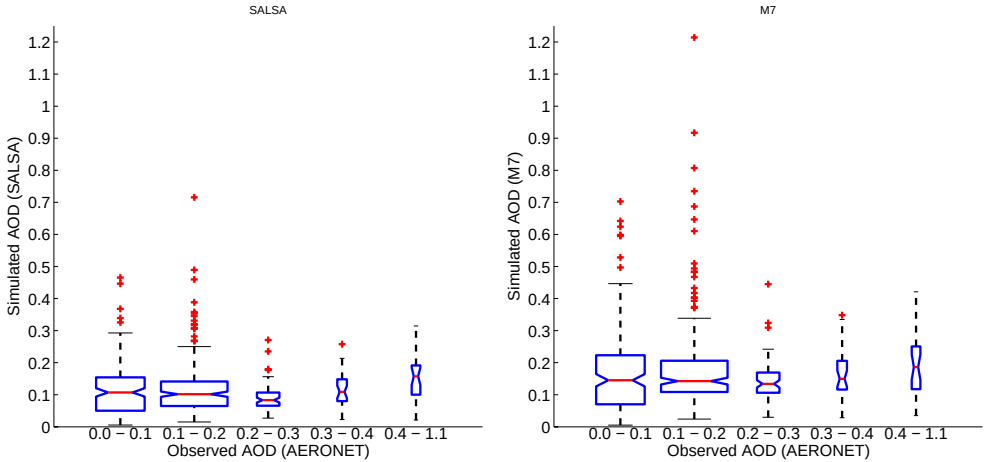


**Fig. 10.** Box plots of simulated AOD at AERONET sites with **(a)** SALSA and **(b)** M7. The box plot shows 25 % and 75 % as the box lower and upper boundaries, and the width of the box indicates the relative amount of data. The line in the box shows the median, and the whiskers show the 95% and 5 % percentiles. The red + signs show the simulated values outside the accepted range (1.5 times the interquantile range). The simulated AODs are grouped to five classes according to observed AOD.





GMDD
4, 3623–3690, 2011



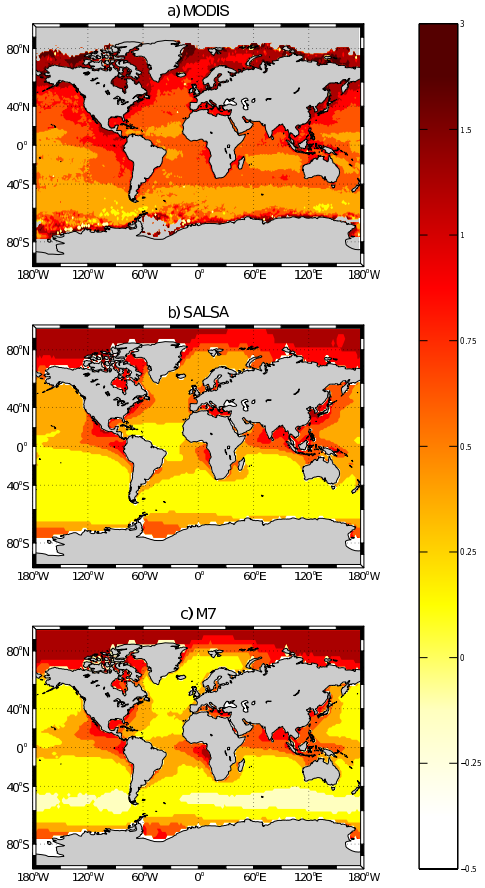


**Fig. 11.** Simulated and satellite retrieved annual mean Ångström exponent of MODIS(550/865 nm), SALSA(550 nm/825 nm) and M7(550 nm/825 nm) for year 2008. Gray areas either have no data or have been omitted.





GMDD
4, 3623–3690, 2011